PHYSICAL REVIEW E **106**, 015110 (2022)

Transient electrohydrodynamics of a liquid drop: The interplay of fluid flow evolution and dynamic response, and the density ratio effects

Asghar Esmaeeli [*]

School of Mechanical, Aerospace, and Materials Engineering, Southern Illinois University, Carbondale, Illinois 62901, USA

(Received 22 September 2021; revised 31 May 2022; accepted 5 July 2022; published 26 July 2022)

Computer simulations are performed to study some of the less explored aspects of the transient electrohydrodynamics of a liquid drop in uniform DC electric fields. The governing equations of the problem are solved using a parallelized front tracking/finite difference method in the framework of Taylor-Melcher's leaky dielectric theory. For density- and viscosity-matched fluid systems, the evolution of the flow field at a high Ohnesorge-squared number $\mathrm{Oh}^2 = \mu^2/\gamma\rho a$ is studied. It is shown that the instantaneous flow pattern is the result of superposition of deformation- and hydrodynamic shear-driven vortices, and that depending on the placement of the fluid systems on the deformation-circulation map, there exists two different paths for the development of the velocity field toward steady state. Examination of the steady-state flow patterns shows that the location of the maximum velocity can shift from the (classically known) drop surface to inside the drop along the poles. The effect of Oh^2 on the dynamic response of the drop and the kinetic energy of the fluid is studied. For high Oh^2 number flows, the dynamic response is monotonic while the kinetic energy evolves in a nonmonotonic way, achieving a distinct peak before settling to steady state. However, for low Oh^2 number flows, both the dynamic response and kinetic energy are oscillatory. Inspection of the results show a two-way coupling between the deformation rate and the fluid flow. The effect of the density ratio $\tilde{\rho} = \rho_i/\rho_o$ (drop to ambient) on the dynamic response and fluid flow strength shows that for high Oh^2 number flows both parameters remain essentially intact at steady state, while their evolution modes transition from a monotonic response to an oscillatory one at high density ratio. However, for low Oh^2 number flows, with an increase in $\tilde{\rho}$, the oscillation frequency of both parameters remain intact, while their oscillation amplitudes increase.

DOI: 10.1103/PhysRevE.106.015110

I. INTRODUCTION

Electrohydrodynamics (EHD) of a liquid drop in uniform DC electric fields has been the focus of increased attention in recent years because of its relevance in a host of technologically advanced and natural processes. The theoretical model that describes the phenomenon fairly well is the so-called Taylor-Melcher leaky dielectric model (LDM) [1,2]. Briefly, under a weak electric field, the drop elongates in the direction of or perpendicular to the electric field, becoming a prolate or an oblate spheroid, respectively. It can also remain spherical, which is a possibility for leaky dielectric fluids because of intricate interplay of electric and hydrodynamic stresses. The electric field also establishes a circulatory flow in and around the drop, whose direction depends on the relative importance of the electric conductivity ratio $\tilde{\sigma} = \sigma_i/\sigma_o$ and the electric permittivity ratio $\tilde{\epsilon} = \epsilon_i/\epsilon_o$ (drop fluid/ambient fluid). For $\tilde{\sigma} < \tilde{\epsilon}$, the direction of the ambient fluid is from the poles (aligned in the direction of the electric field) to the equator, while for $\tilde{\sigma} > \tilde{\epsilon}$ it is the opposite; for $\tilde{\sigma} = \tilde{\epsilon}$, the fluid flow cease to exist, since this is tantamount to a perfectly dielectric drop suspended in another perfect dielectric fluid. As the electric field increases, the drop continues to elongate more or move along a hysteresis curve, where a small increase in the electric field strength at the turning point results in a sudden jump in the deformation, or disintegration of the drops; see, for example, Lac and Homsy [3].

Taylor's analytical solution was extended by several authors to account for the transient period during which the drop and the flow field evolve toward their steady states. Sozou's theoretical study [4] was, perhaps, the first in this regard, who solved the creeping flow equations semi-analytically, while retaining the local fluid acceleration term $\partial\mathbf{u}/\partial t$. The focus of this study was on the evolution of the flow field toward the steady state. The author considered a fluid system for which $\tilde{\epsilon} > \tilde{\sigma}$ (although he did not provide the actual $\tilde{\sigma}$ and $\tilde{\epsilon}$) and showed that the flow structure around the drop initially consisted of closed streamlines that crossed the drop, which first penetrated into it and then gradually retreated into the ambient, leading to the steady flow pattern depicted in the inset of Fig. 2 for region **III**. For this flow, the inner and outer Ohnesorge numbers were (discerned to be) $\mathrm{Oh}_i = \mu_i/\sqrt{\rho_i a\gamma} = 12.9$ and $\mathrm{Oh}_o = \mu_o/\sqrt{\rho_o a\gamma} = 25.8$. To provide a simple closed form solution, Esmaeeli and Sharifi [5] ignored the local acceleration term and showed that the deformation-time curve was monotonic, with the capillary timescale $\mu_o a/\gamma$ being the only characteristic timescale of the problem.

In both of these studies [4,5], however, it was assumed that the surface charge build up was instantaneous, thus, reducing the charge conservation equation to the Laplace equation for

---

[*] esmaeeli@engr.siu.edu

the electric potential. Lanauze *et al.* [6] built on the Sozou's solution and derived an analytical solution that accounted for the effect of surface charge relaxation $\partial q_s/\partial t$. The authors characterized their results in terms of the Ohnesorge number $\mathrm{Oh} = \mu/\sqrt{\rho a\gamma}$ and the Saville number $\mathrm{Sa} = \epsilon\nu/\sigma a^2$, representing the ratios of the capillary timescale $\mu a/\gamma$ and the charge relaxation timescale ϵ/σ to the momentum diffusion a^2/ν timescale, respectively. It was shown that the drop would deform monotonically if charge and momentum relaxation occurred quickly compared to interface deformation, i.e., $\mathrm{Oh} \gg 1$ and $\mathrm{Sa} \ll 1$ for the droplet and medium. However, if $\mathrm{Sa} > 1$ or $\mathrm{Oh} < 1$ for either phase, then the deformation-time curve would be nonmonotonic. Furthermore, the droplet and medium behaved as perfectly dielectrics at early times, which always favored an initial prolate deformation. Zhang, Zahn, and Lin [7] accounted for large drop deformation in strong electric fields, using a spheroidal coordinate system. They ignored the local acceleration term $\partial\mathbf{u}/\partial t$ but accounted for the surface charge relaxation $\partial q_s/\partial t$. Das and Saintillan [8] solved the complete surface conservation equation, using a small-deformation theory. The review article by Vlahovska [9] provides an insightful summary of the state of understanding of the transient electrohydrodynamics of liquid drops and vesicles.

The common limitation of the aforementioned studies is their disregard for the convective effects in the momentum equation. However, to account for them, one needs to resort to higher order analytical solutions or direct numerical simulations (DNSs). In this article, the focus is primarily on the transient behavior of the drops, which is studied using DNSs. Thus, while in the formulation the convective effects are accounted for, the effect of the Ohnesorge number $\mathrm{Oh} = \mu/\sqrt{\rho a\gamma}$, rather than the fluid Reynolds number $\mathrm{Re}_f = ua/\nu$, on the drop behavior and fluid flow is examined. Two notable studies that have examined the Reynolds number effect in a steady-state setting are Refs. [10] and [11].

Finite Reynolds number computational studies concerning the transient behavior of a drop have a relatively short history, but are quickly becoming a routine undertaking. A recent article by Esmaeeli and Behjatian [12] summarizes the state of understanding of the problem for density-matched fluid systems and in the absence of surface charge relaxation and convection. Briefly, at low electric field strength, the dynamic response of the drop is similar to that of a first- (inertia-less) or a second-order (nonzero inertia) mass-damper-spring mechanical system, depending on $\mathrm{Oh}^2 = \mu_o^2/\gamma a\rho_o \gg 1$ or $\mathrm{Oh}^2 \ll 1$, respectively, where the drop settles to a steady deformation $\mathcal{D}_{\mathrm{ss}}$ monotonically [13] or through oscillations [14,15]. However, at higher electric field strength, the dynamic response becomes nonlinear and deviates from that of a mechanical system. Furthermore, for low electric field strength, the Ohnesorge squared number Oh^2 and the viscosity ratio $\widetilde{\mu}$ are the key parameters that determine the transition from a monotonic response to an oscillatory one (and vice versa).

In the experimental and theoretical studies so far, several key aspects of the electrohydrodynamics of a drop have been less explored or have not been explored at all. These include (i) the two-way coupling between the deformation rate and the fluid flow, (ii) the manner in which fluid flow develops toward steady state in the three regions of the deformation-circulation map (Fig. 2) and the mechanism behind the fluid flow development, (iii) the effect of the Oh^2 number on the dynamic response of the drop and the evolution of the kinetic energy, and the time and velocity scales that properly characterize high and low Oh^2 fluid flows, and (iv) the effect of the density ratio $\widetilde{\rho} = \rho_i/\rho_o$ on the dynamic response of the drop and the fluid flow strength, and the time and velocity scales that properly characterize high and low density ratio flows. The major goal of this study is to shed some light on these questions. This is achieved by considering the evolution of the flow field for three representative fluid systems. The motivation is derived from the fact that the electrohydrodynamic-driven flows find relevance in a host of applications, such as enhancement of mixing by chaotic advection [16–19] and heat transfer enhancement by convection [20]. The fluid flow evolution and the effect of the transient fluid inertia has been explored by several authors [4–6]. However, these studies did not examine the two-way coupling of the deformation rate and the fluid flow. Similarly, the majority of the studies that have been carried out so for dealt with density-matched fluid systems, and in a handful of them in which the density of the two fluids were different, the density ratio did not come to the picture since the ambient fluid was a gas, which was dynamically inactive. See, for example, Refs. [13,21,22]. The density ratio effects can come to the picture, for example, in the studies concerning the manipulation of drops in pressure-driven flows [23].

In this study, DNSs are used to investigate the problem. The computer code is based on a well-established methodology that has been used in the past to predict the behavior of a host of multiphase flow problems in the absence of the electric field [24]. In the context of the electrohydrodynamics of drops, detailed information regarding the mathematical formulation and numerical method can be found in Refs. [25] and [26]. The governing equations are solved using parallel computing, in conjunction with message passing interface (MPI). The parallel computing algorithm is similar to the one used by [27] but has been modified to account for the incorporation of the electric field equations. Electric fields of moderate strength is considered, so that the drop will not disintegrate or be subjected to electrorotation.

II. PROBLEM SETUP AND NONDIMENSIONAL PARAMETERS

The physical setup of the problem is shown in Fig. 1, depicting an initially uncharged liquid drop in a pool of another liquid. Here, a is the initial drop radius, and ρ, μ, σ, ϵ, and γ, denote, respectively, density, viscosity, electric conductivity, electric permittivity, and surface tension. Both fluids are initially quiescent. The gravity is set zero. The electric field is established by assigning uniform electric potentials ϕ_t and ϕ_b to the top and the bottom walls, respectively. Thus, in the absence of the drop, the electric potential is linear ($\phi \sim z$) and the electric field strength is uniform; i.e., $E_0 \equiv |\mathbf{E}_0| = |\phi_t - \phi_b|/z_l$. The computational domain is periodic in the horizontal directions and wall-bounded in the vertical direction. No-slip and no-through flow boundary conditions are applied to the velocity field at the walls and periodic boundary conditions

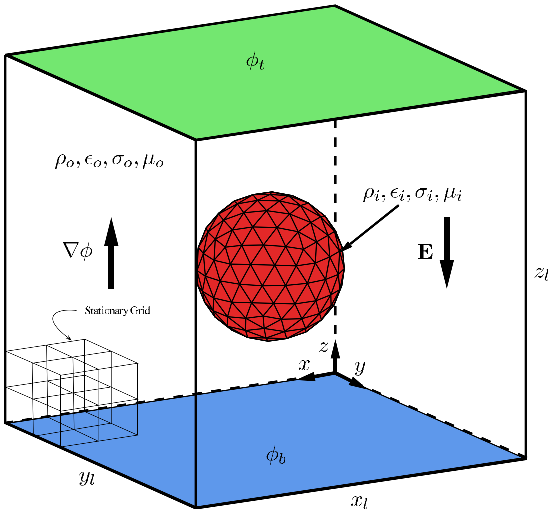

FIG. 1. The computational setup, depicting a liquid drop immersed in another liquid. Here a, ρ, μ, σ, and ϵ represents, respectively, radius, density, viscosity, electric conductivity, and electric permittivity. The computational domain is wall-bounded in the vertical direction and periodic in the horizontal directions. The moving and the fixed grids are also shown schematically.

are used in the horizontal directions. The drop is placed in the middle of the domain. As such, it remains stationary because of the symmetry, while its surface undergoes deformation.

The governing nondimensional numbers of the problem can be best identified by nondimensionalization of the governing equations and their jump conditions. Doing so will put the effect of these numbers and their interplay in perspective. Here, the focus is on the momentum equation since it is controlled by the timescales of the problem. In contrast, the electric field equation $\nabla\cdot(\sigma\nabla\phi)=0$ and the continuity equation $\nabla\cdot\mathbf{u}=0$ are not affected directly by the timescales of the problem. The governing equations can be nondimensionalized in a number of ways based on the choices of the length, time, velocity, and pressure scales. However, each terms in the original equations should be properly scaled and the dimensionless equations should lead to conceptually correct equations in the limits of interest. Three timescales can be identified; the momentum diffusion $\tau_{\mathrm{diff}}=a^2/\nu_o$, the viscous-capillary $\tau_{\mathrm{VC}}=\mu_o a/\gamma$, and the inviscid-capillary timescale $\tau_{\mathrm{IC}}=\sqrt{\rho_o a^3/\gamma}$. It is to be noted that only two of these timescales are independent. The relevant velocity scales are the EHD- and inviscid-capillary (inertiadriven) velocity scales, $u_{\mathrm{EHD}}=\epsilon_o E_0^2 a/\mu_o$ and $u_{\mathrm{IC}}=\sqrt{\gamma/\rho_o a}$, respectively. The former is constructed by balancing the tangential (normal) electric stress $\epsilon_o E_0^2$ with the viscous shear (normal) stress $\mu_o u_{\mathrm{EHD}}/a$ at the drop surface. The latter is found by balancing the dynamic pressure ρu_{IC}^2 with the capillary pressure γ/a. The viscous and inviscid pressure scales are $p_V=\mu_o u_{\mathrm{EHD}}/a=\epsilon_o E_0^2$ and $p_{\mathrm{IC}}=\rho_o u_{\mathrm{IC}}^2=\gamma/a$, respectively. For viscous drops under a low to moderate electric field strength, the relevant time, velocity, and pressure scales are those that are associated with the fluid viscosity; namely, $\tau_{\mathrm{VC}}=\mu_o a/\gamma$ and $\tau_{\mathrm{diff}}=a^2/\nu_o$, $u_{\mathrm{EHD}}=\epsilon_o E_0^2 a/\mu_o$, and $p_V=\mu_o u_{\mathrm{EHD}}/a$. However, to allow for the effect of the surface tension on the fluid acceleration in the momentum equation, one should use the viscous capillary timescale $\tau_{\mathrm{VC}}=\mu_o a/\gamma$ (rather than the diffusion timescale $\tau_{\mathrm{diff}}=a^2/\nu_o$). On dimensional ground, the momentum equation reads

TABLE I. The relevant timescales of the problem. Here, $u_s \equiv u_{\mathrm{EHD}}=\epsilon_o E_0^2 a/\mu_o$.

$\tau_{\mathrm{VC}}=\mu a/\gamma$	$\tau_{\mathrm{diff}}=a^2/\nu$	$\tau_{\mathrm{conv}}=a/u_s$	$\tau_{\mathrm{IC}}=\sqrt{\rho a^3/\gamma}$
viscous-capillary	diffusion	convection	inviscid-capillary

$$\rho_J(\partial\mathbf{u}_J/\partial t+\mathbf{u}_J\cdot\nabla\mathbf{u}_J)=-\nabla p_J+\mu_J\nabla^2\mathbf{u}_J;\ J=i,o. \qquad (1)$$

Considering $\rho_s=\rho_o$, $\mu_s=\mu_o$, $l_s=a$, $u_s=u_{\mathrm{EHD}}$, $t_s=\tau_{\mathrm{VC}}\equiv\mu_o a/\gamma$, and $p_s=p_V\equiv\mu_o u_s/a$ as the density, viscosity, length, velocity, time, and pressure scales, and nondimensionalization of the momentum equation yield

$$\rho_J^*\left(\frac{1}{\mathrm{Oh}^2}\frac{\partial\mathbf{u}_J^*}{\partial t^*}+\mathrm{Re}_f\mathbf{u}_J^*\cdot\nabla^*\mathbf{u}_J^*\right)=-\nabla^* p_J^*+\mu_J^*\nabla^{*2}\mathbf{u}_J^*;$$
$$J=i,o. \qquad (2)$$

In Eq. (2), $\rho_i^*=\rho_i/\rho_o\equiv\widetilde{\rho}$ and $\mu_i^*=\mu_i/\mu_o\equiv\widetilde{\mu}$ are the density and viscosity ratios, $\mathrm{Re}_f=au_s/\nu_o$ is the flow Reynolds number, and $\mathrm{Oh}^2=\mu_o^2/\rho_o a\gamma$ is the Ohnesorge number squared. It is to be noted that $\rho_o^*=1$, $\mu_o^*=1$. Equation (2) presents a proper nondimensionalization of the momentum equation as it allows for the independent scaling of the local acceleration $\partial\mathbf{u}/\partial t$ and the convective $\mathbf{u}\cdot\nabla\mathbf{u}$ terms. Furthermore, this equation converges to the correct form of the momentum equation in the limit of $\mathrm{Oh}^2\to\infty$, i.e., $\rho_J\mathbf{u}_J\cdot\nabla\mathbf{u}_J=-\nabla p_J+\mu_J\nabla^2\mathbf{u}_J$.

In addition to the governing equations, the pertinent jump conditions of the problem should be rendered dimensionless also. Here, capillary number $\mathrm{Ca}=\mu_o u_{\mathrm{EHD}}/\gamma$ emerges as another primary nondimensional number in the process of nondimensionalization of the tangential and normal stress balance; $[\![\tau_{\mathrm{nt}}^e]\!]+[\![\tau_{\mathrm{nt}}^h]\!]=0$ and $[\![\tau_{\mathrm{nn}}^e]\!]+[\![\tau_{\mathrm{nn}}^h]\!]-[\![p]\!]=\gamma\kappa$, respectively.

In summary, the governing nondimensional numbers of the problem are

$$\mathrm{Ca}=\frac{\mu_o u_{\mathrm{EHD}}}{\gamma}\equiv\frac{\epsilon_o E_0^2 a}{\gamma},\quad \mathrm{Oh}^2=\frac{\mu_o^2}{\rho_o a\gamma},$$
$$\widetilde{\sigma}=\frac{\sigma_i}{\sigma_o},\quad \widetilde{\epsilon}=\frac{\epsilon_i}{\epsilon_o},\quad \widetilde{\rho}=\frac{\rho_i}{\rho_o},\quad \widetilde{\mu}=\frac{\mu_i}{\mu_o}. \qquad (3)$$

In addition to Eq. (3), the volume fraction $\alpha=V_d/\Omega$ (V_d and Ω being the volume of the drop and the computational domain, respectively) can influence the results if the computational domain is not sufficiently large. Sometimes in the literature, the nondimensional electric field strength, and the flow Reynolds number the nondimensional electric field strength $E^*=E_0/\sqrt{\gamma/\epsilon_o a}=\sqrt{\mathrm{Ca}}$ and the flow Reynolds number $\mathrm{Re}_f=u_{\mathrm{EHD}}a/\nu_o$ are used in lieu of Ca and Oh, respectively. It is to be noted that $\mathrm{Re}_f=\mathrm{Ca}/\mathrm{Oh}^2$.

The evolution of the drop and the flow field is controlled by several characteristic times (Table I). As such, the relative importance of them can be best understood by representing the governing nondimensional numbers in terms of the ratios of these characteristic times. This yields

$$\mathrm{Oh}^2 = \frac{\tau_{\mathrm{VC}}}{\tau_{\mathrm{diff}}} \equiv \frac{\mu_o a/\gamma}{a^2/\nu_o}; \quad \mathrm{Ca} = \frac{\tau_{\mathrm{VC}}}{\tau_{\mathrm{conv}}} \equiv \frac{\mu_o a/\gamma}{a/u_{\mathrm{EHD}}};$$
$$\mathrm{Re}_f = \frac{\tau_{\mathrm{diff}}}{\tau_{\mathrm{conv}}} \equiv \frac{a^2/\nu_o}{a/u_{\mathrm{EHD}}}. \tag{4}$$

III. MATHEMATICAL FORMULATION AND NUMERICAL METHOD

The governing equations are solved using parallel computing, in conjunction with message passing interface (MPI). The computer code is based on a well-established methodology that has been used in the past to predict the behavior of a host of multiphase flow problems, in the absence of the electric field [24]. In the context of the electrohydrodynamics of drops, detailed information regarding the mathematical formulation and numerical method can be found in Refs. [25], [26], and [12]. Figure 1 summarizes the computational approach. Briefly, rather than writing the governing equations separately for each fluid, a "one-fluid" formulation is used, where a single set of equations is used to represent both fluids, and the phase boundary is treated as an embedded interface by adding the appropriate source terms to the conservation laws. Here, the drop is represented by triangular elements (Lagrangian grid) and the field variables are computed on a fixed (Eulerian) grid. The computational domain is wall-bounded in the vertical direction and periodic in the horizontal directions. The stationary grid is used to discretize the governing equations, and the moving grid marks the position of the phase boundary and is used to keep the stratification of material properties sharp and to calculate the surface tension. This grid is also used to advect the interface by interpolating the velocities of the marker points from the regular grid.

In the computations that follow, the drop diameter is $d = 0.4$ and the computational domain is a cube of $2.5d$ a side, which is resolved by a 128^3 grid. Considering the results of the finest grid as the exact solution, the relative errors in steady-state deformation for 32^3, 64^3, and 128^3 grids were 8.3%, 1.8%, and 0.34%, respectively, reflecting the fact that the results are converged for the 128^3 grid.

IV. BACKGROUND

A. Drop deformation in a weak electric field

For slightly deformed drops, the deformation is typically characterized by the Taylor deformation parameter [28]

$$\mathcal{D} = \frac{z_{\max} - r_{\max}}{z_{\max} + r_{\max}}, \tag{5}$$

which is the difference of the lengths of the axes parallel and perpendicular to the electric field divided by their sum. Using Taylor's solution [1], Vizika and Saville [29] calculated the steady-state drop deformation for slight perturbation from sphericity (Ca $\ll$ 1)

$$\mathcal{D}_{\mathrm{ss}} = \frac{9}{16}\frac{\Phi}{(\widetilde{\sigma}+2)^2}\mathrm{Ca}, \tag{6a}$$

$$\Phi = \underbrace{\widetilde{\sigma}^2 + 1 - 2\widetilde{\epsilon}}_{\Phi^e} + \underbrace{\frac{3}{5}(\widetilde{\sigma} - \widetilde{\epsilon})\frac{3\widetilde{\mu}+2}{\widetilde{\mu}+1}}_{\Phi^h}, \tag{6b}$$

where Φ is the so-called Taylor deformation characteristic function, which determines the sense of drop deformation. For $\Phi < 0$, the drop becomes oblate, while for $\Phi > 0$ it becomes prolate. For $\Phi = 0$ it remains spherical. In Eq. (6), Φ^e and Φ^h represent the contribution of the electric pressure and tangential electric stress in the deformation, respectively.

B. The electric pressure and electric shear stress

The key parameters that determine the sense of interface deformation and fluid circulation are the net normal $[\![\tau^e_{\mathrm{nn}}]\!]$ and tangential $[\![\tau^e_{\mathrm{nt}}]\!]$ electric stresses at the interface, which are also referred to as the electric pressure and the electric shear stress, respectively. Using Maxwell stress tensor $\boldsymbol{\tau}_M = \epsilon\mathbf{EE} - (1/2)\epsilon\mathbf{IE}\cdot\mathbf{E}$ and a normal-tangent coordinate system n-t, it can be shown [30] that

$$[\![\tau^e_{\mathrm{nn}}]\!] = \frac{\epsilon_o}{2}\left[\left(1 - \frac{\widetilde{\epsilon}}{\widetilde{\sigma}^2}\right)E^2_{n_o} + (\widetilde{\epsilon} - 1)E^2_t\right] \tag{7}$$

and

$$[\![\tau^e_{\mathrm{nt}}]\!] = \epsilon_o E_{n_o} E_t\left(1 - \frac{\widetilde{\epsilon}}{\widetilde{\sigma}}\right) = q_s E_t, \tag{8}$$

where

$$q_s = \epsilon_o E_{n_o}\left(1 - \frac{\widetilde{\epsilon}}{\widetilde{\sigma}}\right) \tag{9}$$

is the free electric charge at the surface. Here, $[\![\mathcal{A}]\!] = \mathcal{A}_o - \mathcal{A}_i$ denotes the jump across the drop for a typical parameter $\mathcal{A}$, and subscripts "i" and "o" stand for the inside and the outside.

To analyze the results of the numerical simulations (and for that matter the experimental observations) or to estimate the expected behavior of the drop, scaling arguments have proved to be very helpful. For a moderately deformed drop, the electric pressure at the poles ($\theta = 0$ and π) and the equator ($\theta = \pi/2$), the electric shear stress, and the tangential (surface) velocity can be estimated [3], using Eqs. (7)–(9) in conjunction with the Taylor's solution [1]. This results in

$$[\![\tau^e_{\mathrm{nn}}]\!]^*(0) \sim \frac{9}{2}\frac{\widetilde{\sigma}^2 - \widetilde{\epsilon}}{(\widetilde{\sigma}+2)^2}, \tag{10a}$$

$$[\![\tau^e_{\mathrm{nn}}]\!]^*(\pi/2) \sim \frac{9}{2}\frac{\widetilde{\epsilon} - 1}{(\widetilde{\sigma}+2)^2}, \tag{10b}$$

$$[\![\tau^e_{\mathrm{nt}}]\!]^* \sim \frac{9}{2}\frac{\widetilde{\sigma} - \widetilde{\epsilon}}{(\widetilde{\sigma}+2)^2}, \tag{11}$$

and

$$u^*_t \sim \frac{1}{5}\frac{[\![\tau^e_{nt}]\!]^*}{1+\widetilde{\mu}}, \tag{12}$$

where $\epsilon_o E_0^2$ has been used to render the electric stresses dimensionless. The sense of the deformation can be determined by examination of the electric pressure at the equator and poles, in conjunction with the sense of the fluid flow around the drop. Pole-to-equator flows tend to deform the drop to an oblate, while equator-to-pole flows tend to deform it to a prolate.

C. The electric pressure-, electric shear-, hydrodynamic shear-, and deformation-driven flows

At steady state, where the drop surface is immobile, the fluid flow is due to the electric shear stress $[\![\tau^e_{\rm nt}]\!]$ only. However, the deformation $\mathcal{D}$ is due to both the electric pressure $[\![\tau^e_{\rm nn}]\!]$ and the electric shear stress $[\![\tau^e_{\rm nt}]\!]$. The contribution of the latter to the deformation is due to the normal hydrodynamic stress $[\![\sigma^h_{\rm nn}]\!] \equiv [\![\tau^h_{\rm nn}]\!] - [\![p]\!]$ associated with the shear-driven fluid flow. During the transient, both the electric pressure and electric shear stress contribute to the instantaneous drop deformation and fluid flow. Accordingly, the fluid flow comprises two parts; a part due to instantaneous motion of the interface, and another part due to the interfacial shear stress. To put the roles of these stresses in perspective, it is remarked that in perfectly dielectric fluid systems where the electric shear is absent ($[\![\tau^e_{\rm nt}]\!] = 0$), the fluid flow during the transient is due to the electric pressure only. In this study, the fluid flow due to the deformation rate and the hydrodynamic shear are referred to as the deformation- and hydrodynamic shear-driven flows (or $\partial\mathcal{D}/\partial t$- and $[\![\tau^h_{\rm nt}]\!]$-driven flows), respectively. Here, a distinction is made between the electric shear- and hydrodynamic shear-driven flows, even though the electric shear and hydrodynamic shear are equal (in an absolute sense), $|[\![\tau^e_{\rm nt}]\!]| = |[\![\tau^h_{\rm nt}]\!]|$. In an analytical solution, to examine the electric shear-driven flow, one should set the electric pressure to zero ($[\![\tau^e_{\rm nn}]\!] = 0$) in the normal stress balance $[\![\tau^e_{\rm nn}]\!] + [\![\sigma^h_{\rm nn}]\!] = \gamma\kappa$. However, to examine the hydrodynamic shear-driven flow, one should set $\partial\mathcal{D}/\partial t = 0$ in the formulation (Appendix A). The deformation-driven flow can be found easily by subtracting the $[\![\tau^h_{\rm nt}]\!]$-driven solution from the total solution. It is to be noted that the $[\![\tau^e_{\rm nt}]\!]$- and $[\![\tau^h_{\rm nt}]\!]$-driven solutions will not be the same, and similarly, $[\![\tau^e_{\rm nn}]\!]$- and $\partial\mathcal{D}/\partial t$-driven solutions will not be the same. The deformation-driven flow ceases to exist at steady state where the rate of the deformation is zero. Furthermore, it is due to both the electric pressure and the electric shear stress. However, the shear-driven flow is present even at steady state. The flow structure due to $\partial\mathcal{D}/\partial t$-driven flow will be in line with the local motion of the interface. Thus, the flow direction at the drop surface will be outward (where the interface is expanding into the ambient) and inward (where it is contracting). The flow structure due to the hydrodynamic shear-driven (or $[\![\tau^h_{\rm nt}]\!]$-driven) flow will consist of closed streamlines at the drop surface that do not cross the surface. However, the flow structure due to the electric shear-driven (or $[\![\tau^e_{\rm nt}]\!]$-driven) will consist of streamlines that cross the drop surface during the transient (because of the contribution of the electric shear in the deformation rate). In the next two paragraphs, the original decomposition method (setting $[\![\tau^e_{\rm nt}]\!]$ and $[\![\tau^e_{\rm nn}]\!]$ to zero, sequentially) is compared with the proposed method (setting $\partial\mathcal{D}/\partial t$ and $[\![\tau^e_{\rm nt}]\!]$ to zero, sequentially) in the context of the transient creeping flow solution.

The transient evolution of the drop and the flow field is a two-way coupling phenomenon in which the deformation rate $\partial\mathcal{D}/\partial t$ affects the flow field and vice versa. Major insight about the flow evolution can be gained from the simple closed form solution of Ref. [5]. These authors solved the governing equations of the problem in an asymptotic limit (${\rm Ca} \ll 1$, ${\rm Oh}^2 \gg 1$, and ${\rm Re}_f \ll 1$). In this zeroth-order solution, $r \equiv n$ and $\theta \equiv t$. Taking advantage of the linearity of the governing equations and their jump and boundary conditions, they were able to find the electric pressure- and the electric shear-driven fluid flow and deformation by setting $[\![\tau^e_{r\theta}]\!] = 0$ (in the tangential stress balance) and $[\![\tau^e_{rr}]\!] = 0$ (in the normal stress balance), respectively. The deformation rate was not zero in the electric shear-driven solution because of the normal hydrodynamic stress $[\![\sigma^h_{rr}]\!]$ resulting from the fluid flow. As such, the streamlines crossed the drop surface during the transient. In summary, the total velocity field (stream function) and the deformation could be identified as $\psi = \psi_{\rm EP} + \psi_{\rm ES}$ and $\mathcal{D} = \mathcal{D}_{\rm EP} + \mathcal{D}_{\rm ES}$, using the superposition of the electric pressure- and the electric shear-driven solution. Here, the subscripts EP and ES stand for the electric pressure and electric shear. It is to be noted that the flow structure due to the electric pressure and the electric shear was initially examined by Sozou [4]. However, the solution was not in a closed form.

To characterize how the deformation rate $\partial\mathcal{D}/\partial t$ controls the flow field, the solution of Ref. [5] is recast in a new form by expressing it as a superposition of the deformation- and the shear-driven solutions Eqs. (A1) and (A2). Since in this new expression, the effect of the electric shear stress $[\![\tau^e_{r\theta}]\!]$ in the deformation-driven solution has already been accounted for, the $\partial\mathcal{D}/\partial t = 0$ solution is called the hydrodynamic shear-driven solution. This solution is simply Taylor's steady-state solution [1] since at this zeroth-order $[O({\rm Ca}^0)]$ solution, the impact of the drop deformation on the velocity field is not accounted for.

Examination of the evolution of the forces that control the drop deformation with time provides valuable insight into the problem. The drop deformation $\mathcal{D}$ is the results of interplay of the electric pressure, the normal hydrodynamic stress, and the surface tension, $[\![\tau^e_{rr}]\!] + [\![\sigma^h_{rr}]\!] = \gamma\kappa$. In Ref. [5], both the drop deformation and the fluid flow are controlled by a single timescale ($\tau_{\rm VC} = \mu_o a/\gamma$) only. Thus, both of these entities evolve monotonically. Since the timescale of momentum diffusion is vanishingly small ($\tau_{\rm diff} = a^2/\nu_o \ll 1$), the flow field is established impulsively. Subsequently, the deformation increases (in an absolute sense) and the kinetic energy decreases monotonically until they settle to their steady state.

V. RESULTS AND DISCUSSION

The aim of this study is to investigate some aspects of the electrohydrodynamics of liquid drops that have not been explored or less explored before (Sec. I). The governing nondimensional parameters of the problem are ${\rm Oh}^2$, Ca, α, $\widetilde{\sigma}$, $\widetilde{\epsilon}$, $\widetilde{\mu}$, and $\widetilde{\rho}$ (Sec. II). Here, the volume fraction is fixed at $\alpha = 3.3\%$, corresponding to a drop of radius 0.2 unit in a computational box of unit size. The effect of the confinement on the results will be discussed in Sec. V E. To examine the effect of the dielectric properties ($\widetilde{\sigma}$ and $\widetilde{\epsilon}$) on the results, three fluid systems are considered as the representative fluid systems

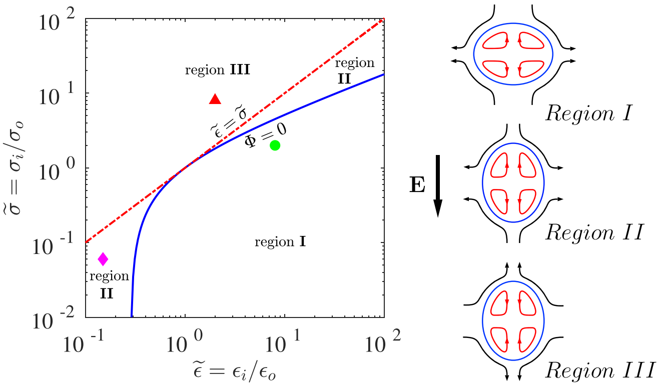

FIG. 2. The circulation-deformation map along with a schematic of the steady-state flow pattern and modes of the drop deformation. The coordinates of the fluid systems *A*–*C* are, respectively, $\widetilde{\epsilon} = 8$, $\widetilde{\sigma} = 2$ (circle), $\widetilde{\epsilon} = 0.15$, $\widetilde{\sigma} = 0.06$ (diamond), and $\widetilde{\epsilon} = 2$, $\widetilde{\sigma} = 8$ (triangle).

from the three regions of the deformation-circulation map. The coordinates of these systems are identified on the map (Fig. 2) and their pertinent information are given in Table II. The representative fluid systems are considered to be density- and viscosity-matched. However, the density ratio $\widetilde{\rho}$ effect is explored by comparing the results with those at $\widetilde{\rho} = 10$ and 100 in Sec. V C. To examine the effect of local fluid acceleration $\partial \mathbf{u}/\partial t$ on the dynamics, $\mathrm{Oh}^2 = 2$ and 0.02 are considered as the limits of small ($\mathrm{Oh}^2 \gg 1$) and large ($\mathrm{Oh}^2 \ll 1$) fluid acceleration, respectively. The justification for considering $\mathrm{Oh}^2 = 2$ as the upper end of the Ohnesorge number comes from the numerical simulations of Ref. [13] who observed marginal differences between the deformation-time curve for $\mathrm{Oh} = 2$ and $\mathrm{Oh} = 200$. Here, the capillary numbers Ca are chosen so that the drop deformation will be modest ($\mathcal{D} \sim 0.1$) for all the reference simulations. The steady-state deformation of the drop is primarily controlled by the product of the modified characteristic function $\widetilde{\Phi} \equiv \Phi/(\widetilde{\sigma}+2)^2$ and the capillary number $\mathrm{Ca} = \mu_o u_s/\gamma$ [Eq. (6)]. For fluid systems *A* and *C*, $\widetilde{\Phi}$ is an order of magnitude larger than that for fluid system *B* (Table II). Thus, an order of magnitude larger capillary number is used for fluid system *B* to obtain a deformation that is nearly the same for all the fluid systems. In summary, two sets of simulations at $\widetilde{\rho} = 1$ are considered as the reference simulations, R_{i_h} and R_{i_l}, where subscript $i = A - C$ refers to the fluid systems and subsubscripts *h* and *l* stand for high ($\mathrm{Oh}^2 = 2$) and low ($\mathrm{Oh}^2 = 0.02$) Ohnesorge square number, respectively. Table III provides pertinent information about the reference simulations.

TABLE II. Pertinent information regarding the fluid systems used in this study. Here, k_1 is the coefficient of the capillary number in $\mathcal{D}_{\mathrm{ss}} = k_1\mathrm{Ca}$, as given in Eq. (6).

Fluid system	Region	$\widetilde{\sigma}$	$\widetilde{\epsilon}$	$\widetilde{\rho}$	$\widetilde{\mu}$	k_1
A	**I**	2	8	1	1	−0.7031
B	**II**	0.06	0.15	1	1	0.0754
C	**III**	8	2	1	1	0.3937

TABLE III. Pertinent information regarding the high- and low-Oh^2 reference simulations. For all the cases, $\widetilde{\rho} = 1$, $\widetilde{\mu} = 1$, $\alpha = 0.035$, and $\mathrm{Re}_{el} = 0.05$.

Reference simulation	Fluid system	Ca	Re_f	$\mathcal{D}$
R_{A_h} (R_{A_l})	*A*	0.2	0.1 (10.0)	~0.1
R_{B_h} (R_{B_l})	*B*	2.0	1.0 (100.00)	~0.1
R_{C_h} (R_{C_l})	*C*	0.2	0.1 (10.0)	~0.1

A. Reference simulations at high Oh^2 number

1. Evolution of the velocity field

The analysis of the problem is initiated by considering the evolution of the fluid flow for high-Oh^2 reference simulations. The pertinent information about these simulations are given in Tables III and IV. Figure 3 shows the velocity field and the drop for reference simulation R_{A_h} at the selected times noted in the caption. The fluid system for this simulation belongs to region **I** of the map. In this figure and the subsequent ones that deal with the velocity field, the velocity vectors in each panel are color-coded according to their relative size $|\mathbf{u}| = \sqrt{u^2+v^2+w^2}$ in that panel, where the minimum and the maximum velocity strengths are represented by the blue and red colors. However, since there is major differences between the strengths of the fluid flow at several stages of the flow evolution, to aid the visualization, the velocity scales in each panel have been set independently and are reported in the caption. In this study, the electric field evolves quasi-steadily since the charge relaxation and convection is ignored, i.e., the Laplace equation $\nabla \cdot \sigma \nabla \phi = 0$ is solved at each time step to determine the electric potential. Thus, the electric field, and hence the electric stresses, are established impulsively. However, the fluid flow is established gradually over a time that is characterized by the momentum diffusion time scale $\tau_{\mathrm{diff}} = a^2/\nu$. The velocity field at a given time is set by the superposition of the deformation- and shear-driven velocity fields (Sec. IV C).

For this fluid system, the electric pressure $[\![\tau^e_{\mathrm{nn}}]\!]$ tends to deform the drop to an oblate Eq. (10). In line with the sense of the deformation, the fluid flow comprises of vortices that cross into the drop surface around the poles and cross out of it around the equator. At steady state where the deformation rate is zero, the net tangential electric stress $[\![\tau^e_{\mathrm{nt}}]\!]$ tends to generate closed vortices that are initiated at the drop surface, and do not cross the surface. The sense of these vortices can be discerned by the relative importance of $\widetilde{\sigma}$ and $\widetilde{\epsilon}$ [Eqs. (11) and (12)]. For $\widetilde{\sigma} < \widetilde{\epsilon}$, the fluid flow around the surface of the drop runs from the poles to the equator, while for $\widetilde{\sigma} > \widetilde{\epsilon}$, it

TABLE IV. The magnitude of the timescales of the high-Oh^2 reference simulations.

Fluid system	$\tau_{\mathrm{VC}} = \mu_o a/\gamma$	$\tau_{\mathrm{diff}} = a^2/\nu_o$	$\tau_{\mathrm{conv}} = a/u_{\mathrm{EHD}}$	$\tau_{\mathrm{IC}} = \sqrt{\rho_o a^3/\gamma}$
A	8.0	4.0	40.0	5.657
B	8.0	4.0	4.0	5.657
C	8.0	4.0	40.0	5.657

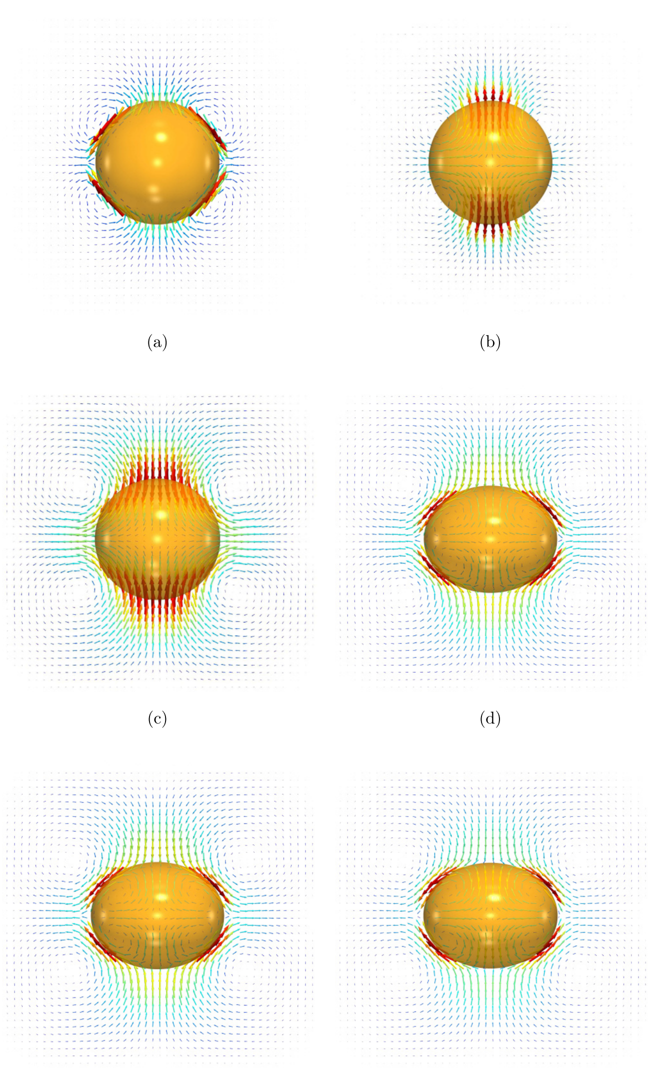
(a) (b)

(c) (d)

(e) (f)

FIG. 3. Evolution of the velocity field toward steady state for reference simulation R_{A_h}. To aid in visualization, the velocity vectors have been scaled independently. The nondimensional time and the velocity scale factor (inside the parentheses) for each panel is (a) 0.00376 (8), (b) 0.0625 (1), (c) 0.375* (1), (d) 2.5 (2), (e) 5 (2), and (f) 15 (2). The times correspond to those marked in Figs. 8 and 9. The asterisk marks the panel for which the kinetic energy is maximum.

runs in the opposite direction. Here, $\widetilde{\sigma} < \widetilde{\epsilon}$, and thus the sense of these vortices is the same as the steady-state flow pattern for region **I** in the inset of Fig. 2. During the transient where the deformation rate is not zero, $[\![\tau^e_{\mathrm{nt}}]\!]$-driven vortices cross the interface. In an unbounded domain, the deformation-driven vortices will be open-ended, except for a small region around their cores (which resides in the ambient fluid). However, because of the confinement effect, here these vortices form closed loops. Panel (a) shows the velocity field at an early time. For this panel, the kinetic energy of the fluid is the minimum (Fig. 8). Thus, to aid visualization, the velocity vectors have been scaled with the maximum scaling. At this early time, the deformation rate is very small. As a result, $[\![\tau^e_{\mathrm{nt}}]\!]$-driven velocity is substantially stronger than $\partial\mathcal{D}/\partial t$-driven velocity, as is evident from the size of the tangent vectors at the drop surface, compared with that of the rest of the velocity vectors. For a liquid drop in a weak electric field and at steady state, the maximum velocity occurs at the drop surface and at polar angles of $\theta = \pi/4$ and $3\pi/4$ radians, measured from the positive z axis [1]. Despite the maximum scaling of the velocity field for panel (a), the velocity field inside the drop is essentially zero, reflecting the fact that the fluid flow has not propagated into the drop yet. As time progresses, the deformation-driven velocity becomes more dominant [panel (b)]. As a result, the tangential velocity vectors are replaced by the velocity vectors that cross into the drop at the poles and cross out of it at the equator [panels (b) and (c)]. Note that the velocity vectors have not been scaled for panels (b) and (c). The kinetic energy of the fluid is maximum for panel (c) (Fig. 8). The flow strength increases with time for panels (a)–(c) but it starts to decrease afterwards until it settles to its steady state where the deformation rate is zero. Compared to panels (a)–(c), in panels (d)–(f) the pace of the evolution of the flow field toward the steady state is relatively slow, since the deformation rate is low. At steady state, the flow field consists of inner and outer vortices that do not cross the drop surface [panel (f)].

While a vector plot of the velocity field at a given time provides useful information about the relative strength of the flow field at different regions of the computational domain, it cannot fully capture the evolution of the flow structure. For instance, in panels (d)–(f), the deformation-driven vortices are gradually retreating to the ambient fluid, while at the same time the recirculating (shear-driven) vortices inside the drop are becoming stronger. However, this information cannot be discerned from the vector plots. To this end, the streamlines, corresponding to the velocity vectors, are presented in Fig. 4. The stream function was found numerically by solving the stream function-vorticity equation in a cylindrical (r–z) coordinates, using the results of the three-dimensional computations. The streamlines at a give time were generally drawn at equispaced values ranging from the minimum value of the stream function to its maximum one. However, occasionally one or two extra contours would be added if the equispaced contours could not capture a weak circulation. Panels (a)–(c) show the penetration of the streamlines into the drop while the flow strength is increasing, and panels (d) and (e) show their retreat to the ambient fluid while it is decreasing. As can be seen from Fig. 9, panels (a)–(c) correspond to the first stage of the drop deformation where the deformation rate (in an absolute sense) is achieving its peak ($\partial^2\mathcal{D}/\partial t^2 > 0$), and panels (d) and (e) corresponds to the second stage where the deformation rate has passed the peak and is gradually diminishing ($\partial^2\mathcal{D}/\partial t^2 < 0$). Here, the initial stage of the flow motion is called the "acceleration stage" and the final stage is called the "deceleration stage." At steady state [panel (f)], the ambient fluid around the drop runs from the poles toward the equator, and no streamline crosses the drop surface, reflecting the fact that the deformation has settled to steady state.

A few remarks regarding the general features of these results can be made. First, in an unbounded domain, the steady-state flow field in the ambient fluid would consist of open vortices. However, because of the domain confinement,

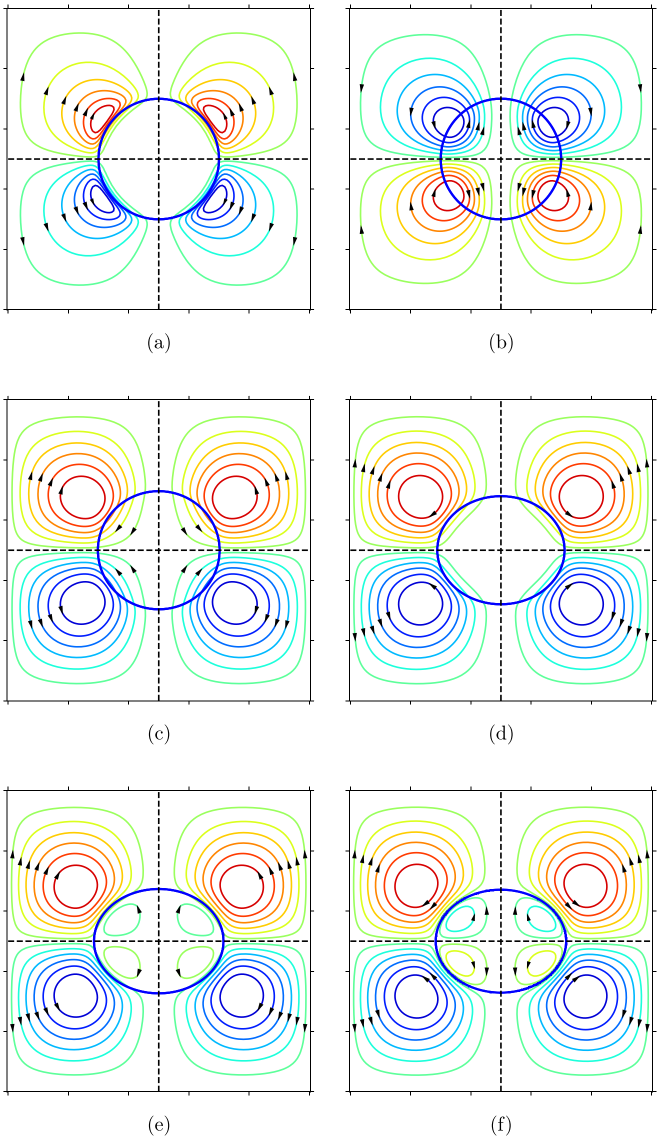
(a) (b) (c) (d) (e) (f)

FIG. 4. Evolution of the velocity streamlines toward steady state for reference simulation R_{A_h}. The nondimensional time for each panel is (a) 0.00376, (b) 0.0625, (c) 0.375* (1), (d) 2.5, (e) 5, and (f) 15. The times correspond to those marked in Figs. 8 and 9. Panels (a)–(c) and (d)–(f) correspond to the acceleration and deceleration stages, respectively. The asterisk marks the panel for which the kinetic energy is maximum.

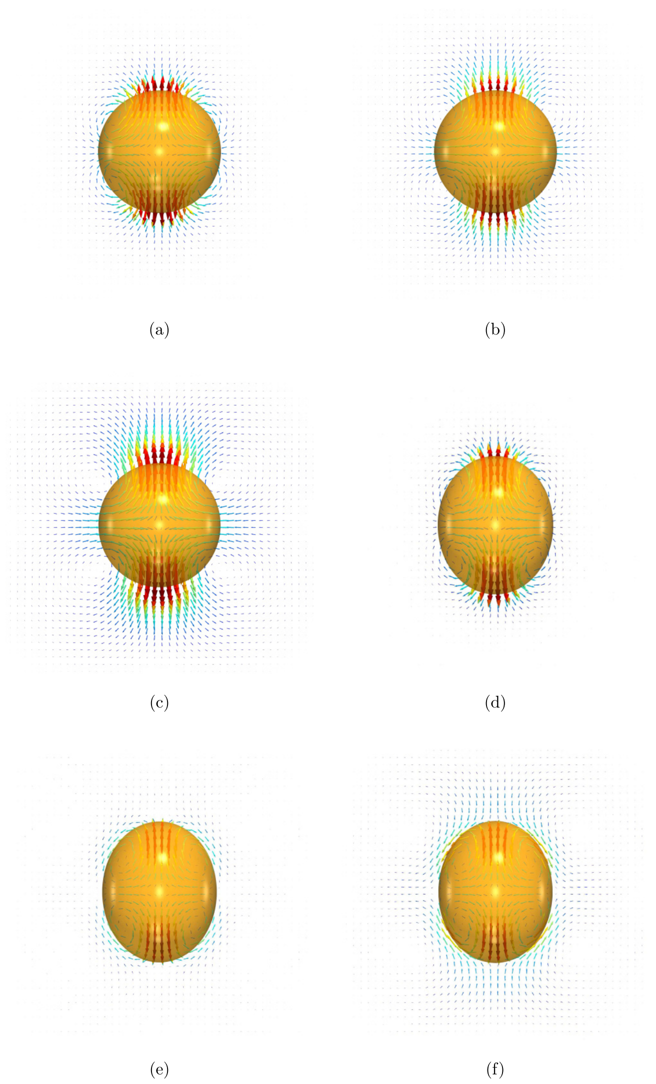
(a) (b) (c) (d) (e) (f)

FIG. 5. Evolution of the velocity field toward steady state for reference simulation R_{B_h}. To aid in visualization, the velocity vectors have been scaled independently. The nondimensional time and the velocity scale factor (inside the parentheses) for each panel is (a) 0.00375 (8), (b) 0.0625 (1), (c) 0.25* (1), (d) 4.0 (3), (e) 6.75 (3), and (f) 22.5 (4). The times correspond to those marked in Fig. 10(a). The asterisk marks the panel for which the kinetic energy is maximum.

here the vortices in the ambient are closed. Second, the plane vortices seen at the steady state [panel (f)] are the cross sections of two toroidal vortices inside the drop in the northern and the southern hemispheres. Third, in the analytical solution [5] where the fluid flow is established instantly, the acceleration stage is bypassed. There, the rate of the deformation is maximum at the outset, and as such, the fluid flow retreats to the ambient from the beginning.

Figure 5 shows the evolution of the velocity field and the drop for reference simulation R_{B_h}. The fluid system for this simulation belongs to region **II** of the map. In this region the electric pressure tends to deform the drop to a prolate Eq. (10), and the creeping flow solution [1] predicts a prolate drop at steady state, even though the fluid flow at steady state tends to deform the drop to an oblate Eq. (11). This is because here the electric pressure $[\![\tau^e_{\mathrm{nn}}]\!]$ is stronger than the electric shear stress $[\![\tau^e_{\mathrm{nt}}]\!]$ [12]. Thus, unlike the simulation for fluid system A, where the $[\![\tau^e_{\mathrm{nt}}]\!]$-driven velocity was dominant at the very beginning, here the deformation-driven flow is dominant at the very beginning [panel (a)]. In line with the instantaneous motion of the drop surface, the deformation-driven vortices cross into the drop surface around the equator and cross out of it around the poles. However, the electric shear stress $[\![\tau^e_{\mathrm{nt}}]\!]$ tends to generate vortices that have the same sense as that of the fluid system A, as the sign of $\widetilde{\epsilon} - \widetilde{\sigma}$ remains unchanged Eq. (11). Here, the velocity fields in panels (a)–(d) are similar, with the only difference between them being the magnitude

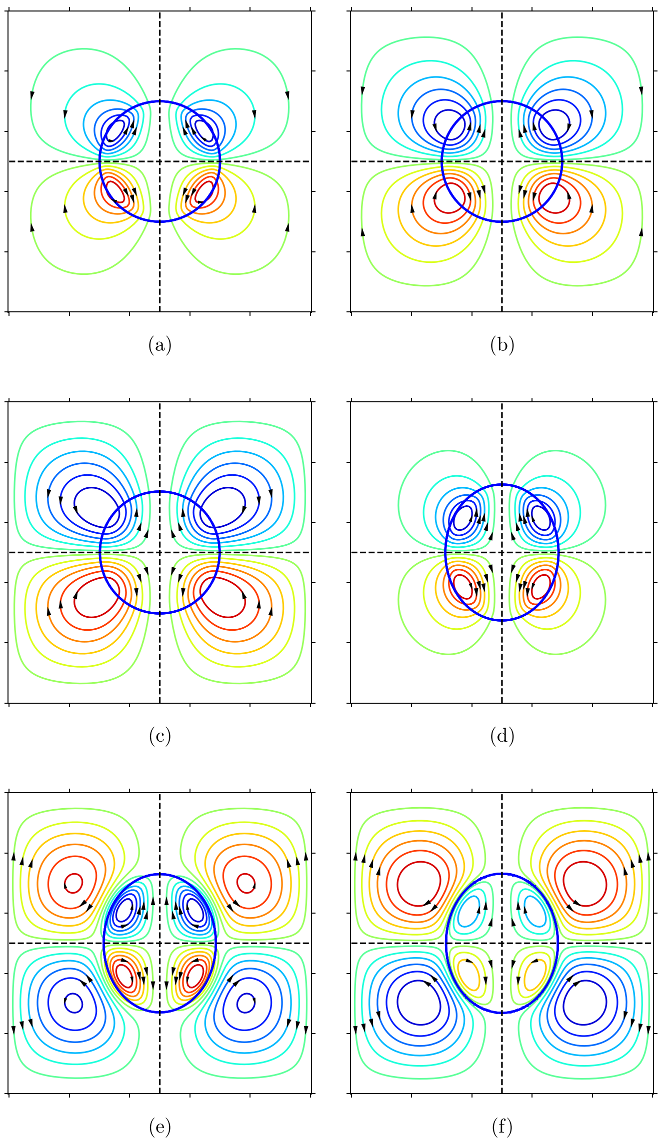

FIG. 6. Evolution of the velocity streamlines toward steady state for reference simulation R_{B_h}. The nondimensional time for each panel is (a) 0.0037, (b) 0.0625, (c) 0.25, (d) 4.0, (e) 6.75, and (f) 22.5. The times correspond to those marked in Fig. 10(a). Panels (a)–(c) and (d)–(f) correspond to the acceleration and deceleration stages, respectively.

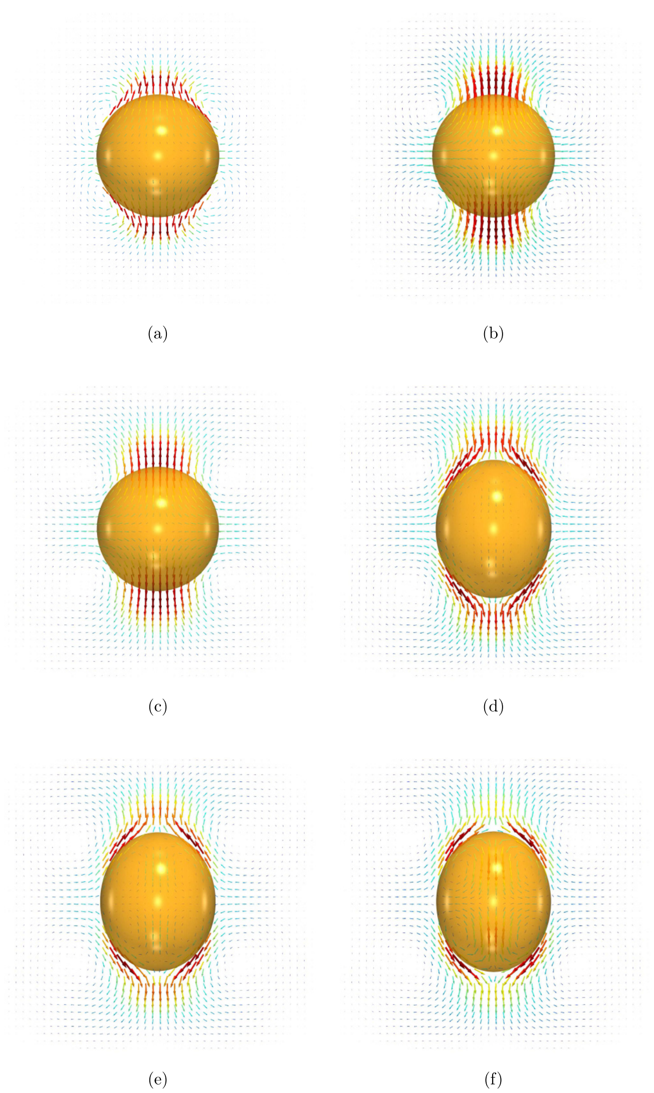

FIG. 7. Evolution of the velocity field toward steady state for reference simulation R_{C_h}. To aid in visualization, the velocity vectors have been scaled independently. The nondimensional time and the velocity scale factor (inside the parentheses) for each panel is (a) 0.00375 (12), (b) 0.0625 (2), (c) 0.375* (1), (d) 7.0 (4), (e) 8.5 (2), and (f) 25 (5). The times correspond to those marked in Fig. 10(b). The asterisk marks the panel for which the kinetic energy is maximum.

of the fluid flow strength [Fig. 10(a)]. Note that the velocity vectors in panels (b) and (c) have not been scaled. The flow strength increases with time for panels (a)–(c) but it starts to decrease afterwards until the deformation rate settles to zero at steady state [Fig. 10(a)]. The senses of flow circulation in and around the drop at steady state are the same as those for fluid system *A* (Fig. 3). Surprisingly, the location of the maximum velocity is inside the drop and along the poles, which is different than that predicted by the classical theory [1]. The discrepancy between the numerical result and the analytical prediction is due to the limitations of the latter, and will be discussed in Sec. V F.

Figure 6 shows the evolution of the velocity streamlines for this simulation. In contrast to the previous simulation (Fig. 4), where the deformation-driven vortices penetrated into the drop during the "acceleration stage" and retreated to the ambient fluid during the "deceleration stage," here these vortices continuously move into the drop. However, they start to lose their strength during the deceleration stage [panels (d)–(f)]. This is evident from the lack of streamlines away from the drop in panel (d), compared to the previous panels. As a result, shear-driven closed vortices are becoming unmasked in the drop and the ambient [panels (e) and (f)]. At the steady state, no streamline crosses into or out of the drop and the fluid around the drop runs from the poles to the equator.

Figure 7 shows the evolution of the velocity field and the drop for reference simulation R_{C_h}. The fluid system for this simulation belongs to region **III** of the map. Here, similarly to fluid system B, the electric pressure tends to deform the drop to a prolate Eq. (10). However, as opposed to fluid systems A and B, the electric shear stress also tends to deform the drop to a prolate. In line with the sense of the deformation, the electric pressure generate vortices that cross into the drop surface around the equator and cross out of it around the poles. Similarly, the electric shear stress tends to generate vortices that have the same sense as those shown in the inset of Fig. 2 for region **III**. Here, at the start of the process, the deformation- and shear-driven velocities are nearly the same order, as is evident from the sizes of the tangential velocity vectors at the drop surface, compared with those of the radial velocity vectors that emanate at the poles [panel (a)]. The flow strength increases for panels (a)–(c), and decreases afterwards until it settles to its steady state [Fig. 10(b)]. The flow strength is at its maximum in panel (c). Note that the velocities in panel (c) have not been scaled. As time progresses, the shear-driven vortices inside the drop become more dominant [panels (d)–(f)]. At steady state, the maximum velocity field appears at the drop surface around the polar angles $\theta = \pi/4$ and $3\pi/4$. The evolution of the velocity streamlines (not shown here) for this simulation was similar to that for R_{A_h}, i.e., the streamlines penetrated into the drop until the rate of the deformation became maximum, and retreated from it, afterward.

A remark is in order regarding the underlying reason for the difference in the observed fluid flow development paths for simulations R_{A_h} (Fig. 4) and R_{B_h} (Fig. 6). In simulation R_{A_h} (as well as R_{C_h}), the sense of shear-driven vortices around the drop surface during the transient was the opposite of the sense of deformation-driven vortices. This opposition led to retreat of the deformation-driven vortices from the drop to the ambient during the deceleration stage. However, for R_{B_h} simulation, the sense of shear- and deformation-driven vortices during the transient were the same. As such, the shear-driven vortices helped to maintain the propagation of the vortices into the drop even during the deceleration stage. It is to be noted that the retreatment of the outer vortices in R_{A_h} and R_{C_h} simulations and their continual penetration into the drop in R_{B_h} simulation provides the only mechanism by which the steady-state fluid flow circulation of Fig. 2 can be realized from the transient vortices with the specified senses.

2. Dynamic response of the drop

The dynamic response of the drop and the fluid flow affect one another. As such, a major insight about their interactions can be gained by examining their evolutions. The dynamic response can be best characterized by considering the deformation-time curve. However, the fluid flow can be characterized by its structure and strength. For fully three-dimensional simulations, the kinetic energy

$$E_k = \frac{1}{2}\int_{\Omega} \rho |\mathbf{V}|^2 d\Omega \tag{13}$$

is a convenient and robust measure to characterize the flow strength, Ω being the volume of the computational domain. Figure 8 shows the evolution of the deformation parameter $\mathcal{D}$ Eq. (5) and the kinetic energy $E_k^* = E_k/E_{k_s}$ ($E_{k_s} = \rho_o u_{\text{EHD}}^2 \Omega$) with the nondimensional time $t^* = t/\tau_{\text{VC}}$, for reference simulation R_{A_h} (Fig. 3). Here, in addition to a linear scale, which is used to show the overall behavior of $\mathcal{D}$ and E_k^*, a semilog scale is used to provide insight into the evolution of these two parameters at an early time. The solid circles on the curves are used to mark the times of the corresponding panels of Fig. 3. From the linear-scale graph it is seen that the deformation parameter increases (in an absolute sense) monotonically and settles to its steady state gradually, while the kinetic energy reaches a peak in a very short period of time, drops down rather rapidly, and then gradually settles to its steady state. Considering the semilog-scale graph, it is seen that the deformation-time curve has an initial tail [curve segment (a)–(b)], along which the deformation is negligibly small. This tail is followed by a curve [curve segment (b)–(f)], along which the deformation initially increases with a fast pace and then settles toward steady state with a slower pace. The kinetic energy-time curve highlights the evolution before and after the peak. Here, the drop is deformed over a time that is set by the viscous capillary timescale $\tau_{\text{VC}} = \mu_o a/\gamma = 8$, while the fluid flow is established over a time that is set by the momentum diffusion timescale $\tau_{\text{diff}} = a^2/\nu_o = 4$. Thus, the fluid flow is established before the drop is fully deformed. Accordingly, the peak in the E_k^*-t^* curve relates to the diffusion timescale τ_{diff}. However, the peak occurs at a shorter time (i.e., $t^*_{\text{max}} = 0.3626 < \tau_{\text{diff}}/\tau_{\text{VC}} = 0.5$), primarily due to the continual fluid flow generation by the electric pressure and the electric shear stress. The kinetic energy does not stay at its peak since it will be controlled by τ_{VC}, which is the dominant timescale. As such, both the deformation and the kinetic energy settle to steady state over the time that is characterized by the viscous-capillary timescale τ_{VC}.

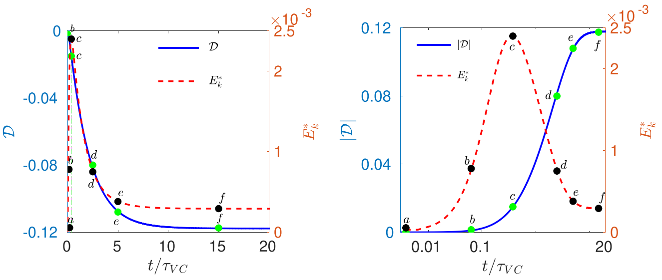

(a) (b)

FIG. 8. Evolution of the deformation parameter $\mathcal{D}$ and the kinetic energy E_k^* for reference simulation R_{A_h} (Table III). The circles identify the times for panels (a)–(f) of Figs. 3 and 4.

The deformation rate is the key parameter behind generation of the fluid flow during the transient. To discern the correlation between this parameter and the kinetic energy, the evolutions of these two parameters with time are presented in Fig. 9. The deformation rate from the analytical solution Eq. (A6) is also added to the figure. The numerical deformation rate-time curve evolves through four stages. It has an initial small tail, along which the rate of the deformation increases slowly. After this tail, the deformation rate starts to increase at a faster pace until it achieves a peak. It then decreases rapidly until the beginning of a final tail, along which it continues to decrease gradually toward steady state. The initial increase in $\partial|\mathcal{D}|/\partial t$ is because of the weak viscous damping, while the momentum gradually diffuses away from the surface of the drop into the drop and the ambient. How-

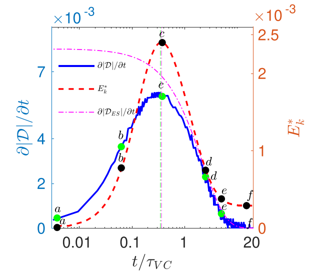

FIG. 9. Evolution of the deformation rate $\partial|\mathcal{D}|/\partial t$ (numerical and analytical [5]) and the kinetic energy E_k^* for reference simulation R_{A_h} (Table III). The circles identify the times for panels (a)–(f) of Figs. 3 and 4.

ever, once the momentum is fully diffused, the deformation rate starts to decrease, leading to the reduction in the flow strength. Here, the weak viscous damping at the beginning does not lead to an oscillatory response since the inertia forces are not strong. The kinetic energy is controlled by the deformation rate, judging by a small time lag that exists between the peak of the former with respect to the latter, i.e., $t^*(\dot{\mathcal{D}}) = 0.347 < t^*_{\max}(E_k^*) = 0.36326$. In the analytical solution [5] where the fluid flow is established instantly, the deformation rate is maximum at the outset and decreases gradually afterwards (Fig. 9).

Figure 10 shows the deformation-time and kinetic energy-time curves for fluid systems B and C. This figure was previously referenced to identify the fluid flow strength of the individual panels of Figs. 5 and 7. It is seen that the evolutions of $\mathcal{D}$ and E_k^* with time are similar to the corresponding ones for fluid system A. However, there are one to two orders of magnitude difference between the the kinetic energy of the three cases, with R_{A_h} and R_{B_h} having the maximum and the minimum kinetic energies, respectively. This observation is in line with that of the creeping flow solution, which predicts that the maximum surface velocity Eq. (A7) for these simulations are $|U_{\max}|/u_s = 0.1688$, 0.0095, and 0.027, respectively. The substantial differences in the fluid flow strength for the three cases are the result of the interplay of the conductivity and the permittivity ratios in setting the electric shear stress Eq. (11), i.e., the flow strength is maximum when $|\widetilde{\epsilon} - \widetilde{\sigma}|$ is maximum and the conductivity ratio $\widetilde{\sigma}$ is minimum. For simulation R_{A_h}, $|\widetilde{\epsilon} - \widetilde{\sigma}|$ is relatively large and $\widetilde{\sigma} = 2$ is modest. However, for simulations R_{B_h} and R_{C_h}, the contrast is weak, and the conductivity ratio is large, respectively.

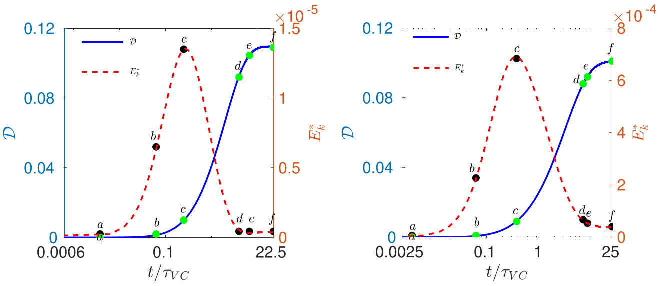

(a)

(b)

FIG. 10. Evolution of the deformation parameter $\mathcal{D}$ and the kinetic energy E_k^* for reference simulations R_{B_h} (a) and R_{C_h} (b). For panel (a), the circles identify the times for panels (a)–(f) of Figs. 5 and 6, while for panel (b), they identify the times for panels (a)–(f) of Fig. 7. Table III provides the information about the fluid systems.

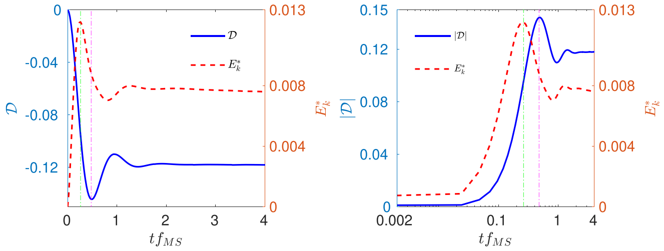

(a)

(b)

FIG. 11. Evolution of the deformation parameter $\mathcal{D}$ and the kinetic energy E_k^* for reference simulation R_{A_l} (Table III), using linear and semilog scales. Here, $f_{\mathrm{MS}} = \omega_{\mathrm{MS}}/2\pi$, where ω_{MS} is given in Eq. (B2b). The kinetic energy is nondimensionalized by $\rho_o u_{\mathrm{MS}}^2 \Omega$, where $u_{\mathrm{MS}} = a\omega/(2\pi)$.

In summary, for high-Oh^2 number reference simulations, the dynamic response was monotonic for all the fluid systems. However, the evolution of the kinetic energy was nonmonotonic. The deformation rate was initially high while the viscous damping was weak, but started to decrease after the viscous force was established. The evolution of the kinetic energy was controlled by that of the rate of the deformation. Here, the dynamic response resembled that of a mass-damper-spring mechanical system ($F_e - (kx + c\dot{x}) = m\ddot{x}$) with a small inertia ($m\ddot{x}$), as it was overdamped. However, the problem was governed by two timescales. On the other hand, in the creeping flow solution of Ref. [5], the inertia was completely ignored. As such, the problem was governed by a single timescale only.

B. Reference simulations at low-Oh^2 number

The monotonic behavior for the deformation-time curve (Fig. 8) will be disrupted if Oh^2 becomes sufficiently small. For the ambient fluid, $1/\mathrm{Oh}^2$ emerges as the parameter that controls the local acceleration term $\partial \mathbf{u}/\partial t$ Eq. (2). However, considering the momentum Eq. (2) for the drop fluid and balancing the first and the last terms suggests that

$$\Pi = \frac{\widetilde{\rho}}{\widetilde{\mu}}\left(\frac{1}{\mathrm{Oh}^2}\right) \tag{14}$$

is the parameter that controls the local acceleration in general. Thus, small Oh^2, as well as large $\widetilde{\rho}$ and small $\widetilde{\mu}$, favors an oscillatory behavior. Generally speaking, smaller Oh^2 number is tantamount to a larger drop or a less viscous surroundings.

For each fluid system, a simulation at Oh$^2 = 0.02$ was performed as a representative of low Oh^2 simulation. However, here the focus will be mostly on fluid system A, since the results for the other fluid systems were similar to those for fluid system A. Furthermore, the evolution of the velocity field is not presented, since the manner in which the fluid flow evolves can be predicted from the corresponding $\mathcal{D}$-t^* and E_k^*-t^* curves that will follow, taking advantage of the insight that was gained from the fluid flow evolution for high Oh^2 simulations (Sec. V A). Figure 11 shows the $\mathcal{D}$-t^* and

TABLE V. Numerical period T_n and analytical estimates of the period along with the magnitude of the timescales for the low-Oh^2 reference simulations. Here, $\omega_s = 1/\tau_{\rm IC}$, where $\tau_{\rm IC} = \sqrt{\rho_o a^3/\gamma}$, and $\omega_{\rm L}$ and $\omega_{\rm MS}$ are given in Eqs. (B2a) and (B2b).

Fluid system	T_n	$T_{\rm IC} = 2\pi/\omega_s$	$T_{\rm L} = 2\pi/\omega_{\rm L}$	$T_{\rm MS} = 2\pi/\omega_{\rm MS}$	$\tau_{\rm IC}$	$\tau_{\rm conv}$	$\tau_{\rm VC}$	$\tau_{\rm diff}$
A	2.0	3.5543	1.622	2.09	0.5667	0.4	0.08	4.0
B	1.9	3.5543	1.622	2.09	0.5667	0.04	0.08	4.0
C	2.7	3.5543	1.622	2.09	0.5667	0.4	0.08	4.0

E_k^*-t^* curves for fluid system A. Compared to the counterpart simulation at high Oh^2 (Fig. 8) where the dynamic response was monotonic, here, the dynamic response is oscillatory. The deformation parameter $|\mathcal{D}|$ has a large initial peak that is followed by a smaller dip, and nearly an imperceptible second peak. The oscillatory behavior of the $\mathcal{D}^*$-t^* curve suggests that a timescale that is constructed based on the frequency of the oscillation will be a more appropriate timescale. The question that arises is what the intrinsic frequency of the problem would be. To provide an answer, the numerical period T_n was first examined by simply measuring the (dimensional) peak to peak distance on the deformation-time curve. Next, the period of oscillation was calculated using three different equations; Eq. (B2a) and (B2b), and the inviscid-capillary timescale $\tau_{\rm IC} = \sqrt{\rho_o a^3/\gamma}$. Here, the first equation is due to Lamb [31], which gives the frequency of small amplitude oscillation of an inviscid drop, while the second equation is based on Miller and Scriven [32], which is also designated for small amplitude oscillation but allows for small viscosity in both fluids (i.e., $\mu_i,\ \mu_o \ll 1$). Table V provides information about the numerical and analytical period as well as the other relevant timescales of the problem. It should be noted that Eq. (B2a) and (B2b) are used outside their range of applicability as the degree of drop deformation is not negligible (i.e., $\mathcal{D} \sim 0.1$). Table V makes it plain that for each fluid system the Miller-Scriven period is the closest period to the numerical period T_n. Accordingly, the timescale of oscillation is governed by this period. However, after the drop goes through a cycle of oscillation, its settling toward the steady state is controlled by the momentum diffusion timescale $\tau_{\rm diff}$, which is also the largest time of the problem (Table V).

To nondimensionalize the kinetic energy, a velocity scale associated with the oscillatory motion should be used. Here, a Miller-Scriven velocity scale [$u_{\rm MS} = a\omega_{\rm MS}/(2\pi)$] is used, as opposed to $u_{\rm EHD} = \epsilon_o E_0^2 a/\mu$, which was used for the high Oh^2 reference simulations. The kinetic energy also settles to its steady state over a time that is characterized by $\tau_{\rm diff}$ (Fig. 11). However, its evolution is not monotonic also since it is controlled by the deformation rate, which is nonmonotonic. This can be verified from Fig. 12, which shows that the kinetic energy has a time lag with respect to the deformation rate. Thus, the deformation rate is the driver behind the variations in the kinetic energy, while the fluid flow controls the deformation parameter, as $\mathcal{D}$ has a time lag with respect to E_k^*. The oscillation period of the deformation is slightly larger than that of the kinetic energy. The peaks of $\partial|\mathcal{D}|/\partial t$, E_k^*, and $|\mathcal{D}|$ occur at $t^*_{\max}(|\dot{\mathcal{D}}|) = 0.1793$, $t^*_{\max}(E_k^*) = 0.2629$, and $t^*_{\max}(|\mathcal{D}|) = 0.4781$.

In summary, for low-Oh^2 number reference simulations, the dynamic response resembled that of an underdamped second order mechanical system for all the fluid systems. For small deformation and nearly inviscid fluids, the Miller-Scriven solution [Eqs. (B1) and (B2)] serves as a good model to characterize the dynamic response. For this solution, the governing timescales are the oscillation period $T_{\rm MS} = 2\pi/\omega_{\rm MS}$ and the damping rate ζ. Considering the scaling arguments, the relevant timescales of the problem were the inviscid capillary $\tau_{\rm IC}$ and the momentum diffusion $\tau_{\rm diff}$ timescales. The kinetic energy evolved nonmonotonically and was controlled by the deformation rate.

C. Effect of the density ratio $\tilde{\rho}$

The density ratio effect on the transient electrohydrodynamics of leaky dielectric drops has not been explored before. The local acceleration term $\partial \mathbf{u}/\partial t$ in the drop fluid (as well as the convective term) correlates positively with $\tilde{\rho}$ Eq. (2). Accordingly, as $\tilde{\rho}$ is increased, one would expect a monotonic dynamic response to transition to an oscillatory one and vice versa. To explore the effect of $\tilde{\rho}$, two simulations at density ratios of $\tilde{\rho} = 10$ and 100 were performed, corresponding to each high- and low-Oh^2 reference simulation. In these simulations, the density ratio was changed by changing the density of the drop fluid ρ_i. As such, for unequal-density simulations, the momentum diffusion timescale $\tau_{\rm diff} = a^2/\nu$ and the inviscid capillary timescale $\tau_{\rm IC} = \sqrt{\rho a^3/\gamma}$ are different for the ambient fluid and the drop fluid, and change from one simulation to another. Accordingly, the more dominant momentum diffusion timescale and inviscid capillary timescale are those associated with the drop fluid ($\tau_{{\rm diff}_i} = a^2/\nu_i$ and $\tau_{{\rm IC}_i} = \sqrt{\rho_i a^3/\gamma}$) as they are larger than their counterparts in the ambient fluid. Here, to characterize the fluid flow strength, the mean fluid velocity,

$$\bar{u} = \sqrt{\frac{1}{\Omega}\int_{\Omega} |\mathbf{V}|^2 d\Omega}, \tag{15}$$

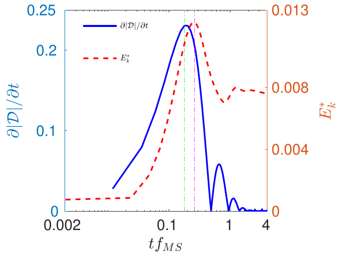

FIG. 12. Evolution of the deformation rate $\partial|\mathcal{D}|/\partial t$ and the kinetic energy E_k^* for reference simulation R_{A_l} (Table III). Here, $f_{\rm MS} = \omega_{\rm MS}/2\pi$, where $\omega_{\rm MS}$ is given in Eq. (B2b). The kinetic energy is nondimensionalized by $\rho_o u_{\rm MS}^2 \Omega$, where $u_{\rm MS} = a\omega/(2\pi)$.

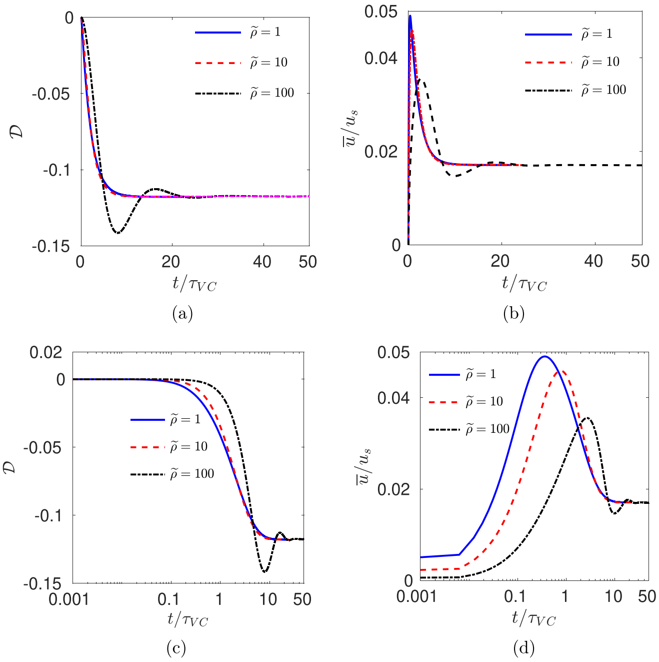

(a) (b)

(c) (d)

FIG. 13. Evolution of the deformation parameter and the mean velocity with time at three density ratios $\widetilde{\rho}$ for high-Oh^2 reference simulation R_{A_h}, using linear and semilog scales. The density ratio $\widetilde{\rho}$ was changed by changing the density of the drop ρ_i. Here, the velocity scale is $u_s = \epsilon_o E_0^2 a/\mu_o$ and the time is nondimensionalized with the viscous-capillary timescale $\tau_{\rm VC} = \mu_o a/\gamma$.

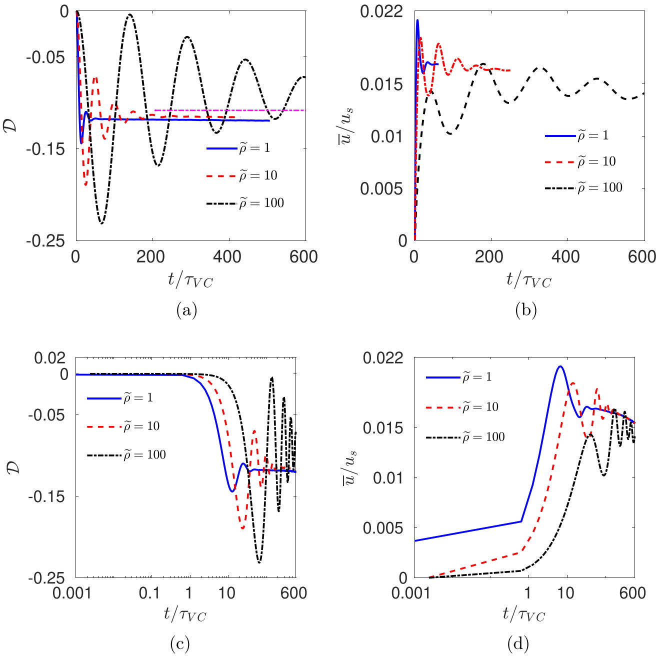

(a) (b)

(c) (d)

FIG. 14. Evolution of the deformation parameter and the mean velocity with time at three density ratios $\widetilde{\rho}$ for low-Oh^2 reference simulation R_{A_l}, using linear and semilog scales. The density ratio $\widetilde{\rho}$ was changed by changing the density of the drop ρ_i. Here, the velocity scale is $u_s = \epsilon_o E_0^2 a/\mu_o$ and the time is nondimensionalized with the viscous-capillary timescale $\tau_{\rm VC} = \mu_o a/\gamma$.

is used instead of the kinetic energy E_k, since this parameter would be a better measure as it bypasses the weighting of the fluid flow strength by the densities.

Figure 13 explores the effect of the density ratios $\widetilde{\rho}$ on the evolution of the deformation parameter $\mathcal{D}$ and the mean velocity $\overline{u}^* = \overline{u}/u_s$ ($u_s = \epsilon_o E_0^2 a/\mu_o$) for the high-Oh^2 reference simulation of fluid system A (h_{A_h}). The corresponding results for fluid systems B and C are not presented here, since they were essentially the same as those shown here. A few observations can be made about this figure. First, an order of magnitude increase in the density ratio from $\widetilde{\rho} = 1$ to 10 does not lead to a tangible difference in the deformation parameter. However, an order of magnitude increase in $\widetilde{\rho}$ from 10 to 100 transitions the monotonic responses to the oscillatory ones for both $\mathcal{D}$ and $\overline{u}^*$. The rather weak impact of $\widetilde{\rho}$ on the dynamic response is presumably due to the fact that this parameter has direct impact on the drop fluid only, which has a much smaller volume than that of the ambient (i.e., the volume fraction is about 3.5%). Second, the steady-state deformation and mean velocity are unaffected by the density ratio. This implies, considering the normal and tangential stress balance, that the normal $[\![\sigma_{\rm nn}^h]\!]$ and the tangential $[\![\tau_{\rm nt}^h]\!]$ hydrodynamic stresses at steady state remain essentially unchanged as a result of the change in the density ratio. Third, while the mean velocity at steady state is unaffected by the changes in the density ratio, it tends to correlate negatively with this parameter during the transient. Furthermore, the time that it takes for the velocity to achieves it peak increases with an increase in the density ratio. Two factors contribute to this: (i) the deformation rate (not shown here) during the acceleration stage decreases with an increase in $\widetilde{\rho}$, (ii) the momentum diffusion time increases with an increase in $\widetilde{\rho}$, i.e., $a^2/\nu_i = 4.0, 40.0,$ and 400.00, for $\widetilde{\rho} = 1$, 10, and 100, respectively. Compared to the low-Oh^2 reference simulations (Table V), here, the Miller-Scriven period does not provide as good of an estimate. This is because the Miller-Scriven solution is valid for Oh$^2 \ll 1$, which is not the case here.

Figure 14 compares the evolution of the deformation parameter $\mathcal{D}$ and the mean velocity $\overline{u}^* = \overline{u}/u_s$ with time at different density ratios $\widetilde{\rho}$ for the low-Oh^2 reference simulation of fluid system A (h_{A_l}). The corresponding results for fluid systems B and C are not presented since they were essentially the same as those shown here. Here, to scale the frequency of oscillation and fluid flow strength uniformly for all the simulations, the time and the velocity scales have been nondimensionalized with $\tau_{\rm VC} = \mu_o a/\gamma$ and $u_{\rm EHD} = \epsilon_o E_0^2 a/\mu_o$, both of which are independent of the density ratio. The highly oscillatory nature of the $\widetilde{\rho} = 100$ curves is due to the simultaneous effect of $\widetilde{\rho}$ and Oh^2, which is characterized by Eq. (14). Two observations can be made. First, the dynamic response is oscillatory at all the density ratios. However, the oscillation frequency ($\mathcal{D} - t$ curve) decreases with an increase in the density ratio, while the oscillation amplitude increases. Inspection of the results shows that the oscillation frequency of the deformation parameter $\mathcal{D}$ and that of the mean velocity $\overline{u}$ are nearly the same. Second, the time-averaged deformation $\overline{\mathcal{D}}$ increases with an increase in $\widetilde{\rho}$. The changes are more pronounced when $\widetilde{\rho}$ is increased from 10 to 100, compared to those for which $\widetilde{\rho}$ is increased from 1 to 10. Contrary to the $\mathcal{D} - t$ curve, the time-averaged mean velocity $\overline{\overline{u}}$ decreases

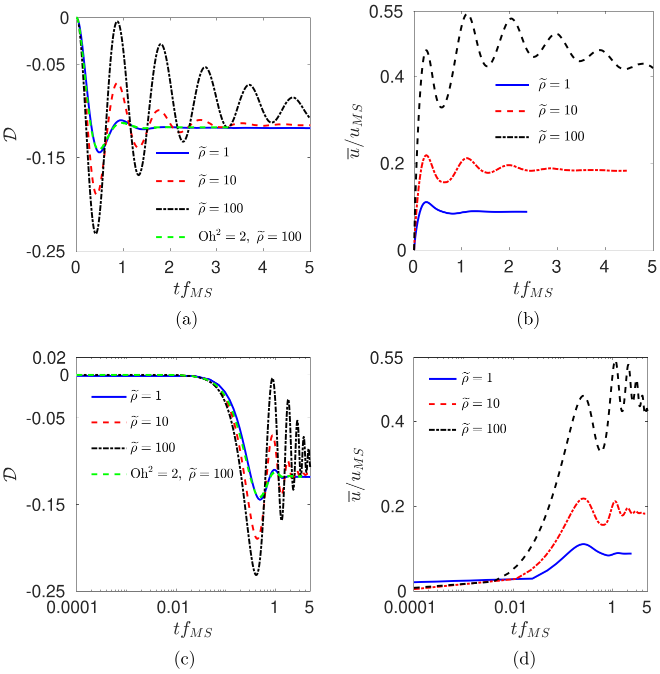

FIG. 15. Evolution of the deformation parameter and the mean velocity with time at three density ratios $\widetilde{\rho}$ for low-Oh^2 reference simulations R_{A_l}, using linear and semilog scales. The density ratio $\widetilde{\rho}$ was changed by changing the density of the drop ρ_i. Here, $f_{\mathrm{MS}} = \omega_{\mathrm{MS}}/2\pi$ and the velocity scale is $u_{\mathrm{MS}} = af_{\mathrm{MS}}$, where ω_{MS} is given in Eq. (B2b).

with an increase in $\widetilde{\rho}$, which is primarily due to the decrease in the deformation frequency. Inspection of the evolution of the mean velocities inside ($\overline{u}_i$) and outside ($\overline{u}_o$) of the drop (not shown here) showed that these quantities followed the similar trend as that for the mean velocity of the whole flow field ($\overline{u}$).

Because of the oscillatory behavior of the curves in Fig. 14, a more appropriate scaling would be those associated with Miller-Scriven scales. Figure 15 is the result of this rescaling. As opposed to Fig. 14, here, the nondimensional frequencies of the three curves are nearly the same. This observation reaffirms the fact that the Miller-Scriven frequency f_{MS} is the intrinsic frequency of the problem. Furthermore, contrary to Fig. 14, here the nondimensional mean velocity increases with an increase in $\widetilde{\rho}$. The result for $\mathrm{Oh}^2 = 2\ (\widetilde{\rho} = 100)$ simulation has been also added to the $\mathcal{D} - t^*$ curve (nondimensionalized by its own Miller-Scriven frequency f_{MS} from Table VI), where it is seen that $\mathcal{D} - t^*$ curves for $\mathrm{Oh}^2 = 2\ (\widetilde{\rho} = 100)$ and $\mathrm{Oh}^2 = 0.02\ (\widetilde{\rho} = 1)$ simulations are essentially the same. This observation suggests that for the range of the parameters used, the convective effects do not play a role in the deformation $\mathcal{D}$, since there is a two order of magnitudes difference between $\rho_o^*\mathrm{Re}_f$ (which scales the convective term in the ambient) for the corresponding simulations, i.e., $\rho_o^*\mathrm{Re}_f = 1 \times 0.1 = 0.1$ for $\mathrm{Oh}^2 = 2\ (\widetilde{\rho} = 100)$ and $\rho_o^*\mathrm{Re}_f = 1 \times 10 = 10$ for $\mathrm{Oh}^2 = 0.02\ (\widetilde{\rho} = 1)$. Note that $\rho_i^*\mathrm{Re}_f$ (which scales the convective term in the drop) is the same (i.e., 10) for both simulations (Table III). Table VII compares the relevant timescales with the numerical period for this simulation and the corresponding ones for fluid systems B and C (not shown here).

TABLE VI. Numerical period T_n and analytical estimates of the period for high Oh^2 simulations at $\widetilde{\rho} = 100$. Here, $\omega_{s_i} = 1/\tau_{\mathrm{IC}_i}$, where $\tau_{\mathrm{IC}_i} = \sqrt{\rho_i a^3/\gamma}$, and ω_{L} and ω_{MS} are given in Eqs. (B2a) and (B2b).

Fluid system	T_n	$T_{\mathrm{IC}_i} = 2\pi/\omega_{s_i}$	$T_{\mathrm{L}} = 2\pi/\omega_{\mathrm{L}}$	$T_{\mathrm{MS}} = 2\pi/\omega_{\mathrm{MS}}$	τ_{IC_i}	τ_{diff_i}
A	127.90	355.43	126.08	134.07	56.57	400
B	144.90	355.43	126.08	134.07	56.57	400
C	187.90	355.43	126.08	134.07	56.57	400

D. Predicting the dynamic response at the outset

From the investigations so far it is clear that the key parameters that determine the transition from a monotonic response to an oscillatory one (or vice versa) for viscosity-matched fluid systems are the Ohnesorge number squared Oh^2 and the density ratio $\widetilde{\rho}$. A question that naturally arises is how to predict the dynamic response *a priori* for a given Oh^2 and $\widetilde{\rho}$. This question can be answered by considering Eqs. (5.9) and (5.10) of Ref. [12], which characterizes the dynamic response of a liquid drop for small deformation at arbitrary Oh^2. Considering those equations, the transition from a monotonic response to an oscillatory one is determined by the magnitude of $\tau\omega_{\mathrm{L}}/2$ relative to one, where τ is the time constant (A6b) and ω_{L} is the Lamb inviscid frequency (B2c). Accordingly, setting $\tau\omega_{\mathrm{L}}/2 = 1$ leads to the characteristic Ohnesorge number (squared)

$$\mathrm{Oh}_c^2 = \frac{3\widetilde{\rho}+2}{6}\left[\frac{40(\widetilde{\mu}+1)}{(19\widetilde{\mu}+16)(2\widetilde{\mu}+3)}\right]^2, \tag{16}$$

for which the dynamic response switches from an overdamped response ($\mathrm{Oh}^2 > \mathrm{Oh}_c^2$) to an underdamped one ($\mathrm{Oh}^2 < \mathrm{Oh}_c^2$). Considering the fact that Oh_c^2 is a decreasing function of $\widetilde{\mu}$ and an increasing function of $\widetilde{\rho}$, and that a higher Oh_c^2 is tantamount to a liquid drop that more readily becomes oscillatory, all things being the same, the oscillatory behavior is favored toward the drops that are less viscous and more dense than the surrounding fluid. Figure 16, which is based on Eq. (16), provides a map that can be used at the outset to predict the mode of the dynamic response. Here, the symbols represent the placement of high- and low-Oh^2 simulations on this map using Eq. (16). The theoretical prediction matches with the numerical results, lending support to Eq. (16).

E. Confinement effect

In the majority of the numerical and analytical studies so far, the ambient fluid has been considered to be essentially unbounded. See, for example, Refs. [3,6,10,33]. In the current study, however, the computational domain was finite. The domain confinement can affect the results in a qualitative and a quantitative way. Qualitatively, the streamlines in the ambient fluid will form closed loops (Figs. 4 and 6), as opposed to those in an unbounded domain, which are open-ended (e.g., Fig. 1 of Ref. [1]). Quantitatively, the confinement can affect the degree of drop deformation and fluid flow strength. For steady-state creeping flows ($\mathrm{Ca} \ll 1$, $\mathrm{Re}_f \ll 1$), Ref. [34]

TABLE VII. Effect of density ratio $\widetilde{\rho}$ on the oscillation period for $\mathrm{Oh}^2 = 0.02$ simulations. Here, $\omega_{s_i} = 1/\tau_{\mathrm{IC}_i}$ and $u_{\mathrm{IC}_i} = a/\tau_{\mathrm{IC}_i}$ where $\tau_{\mathrm{IC}_i} = \sqrt{\rho_i a^3/\gamma}$, and ω_{L} and ω_{MS} are given in Eq. (B2a) and (B2b).

$\widetilde{\rho}$	T_n $(A\ B\ C)$	$T_{\mathrm{IC}_i} = 2\pi/\omega_{s_i}$	$T_{\mathrm{L}} = 2\pi/\omega_{\mathrm{L}}$	$T_{\mathrm{MS}} = 2\pi/\omega_{\mathrm{MS}}$	τ_{IC_i}	u_{IC_i}	τ_{diff_i}
1	2.0 1.9 2.70	3.5543	1.622	2.09	0.5657	0.4180	4.0
10	3.90 4.50 5.50	11.2397	4.10	4.4844	0.8969	11.2397	40.0
100	10.5 13.60 16.50	35.543	12.60	12.85	2.57	35.543	400.0

explored the confinement effect by solving the electrohydrodynamic equations analytically, considering a liquid drop of radius a, suspended in a pool of another liquid in a spherical rigid container of radius b, where the drop and the container were concentric. Accordingly, they examined the confinement effect by evaluating the effect of the so-called confinement ratio $\lambda = a/b$ on the results. The results of this study showed that depending on the relative importance of the ratio of the dielectric properties $(\widetilde{\sigma}, \widetilde{\epsilon})$ and the viscosity ratio $\widetilde{\mu}$, the fluid flow strength (characterized by the maximum surface velocity $U_{\max}$) and the deformation $\mathcal{D}$ would correlate positively or negatively with $\lambda = a/b$. It is to be noted that the confinement ratio is related to the volume fraction through $\lambda = \alpha^{1/3}$.

Table VIII provides information regarding the confinement effect on the steady-state deformation $\mathcal{D}$ and the maximum surface velocity $U_{\max}$ for all the fluid systems, using creeping flow solution [34]. Here, $\mathcal{D}_\infty$ and $U_{\max_\infty}$ are the corresponding results for an unbounded domain [1] (i.e., $\lambda = 0$), while the results for the confined domain corresponds to $\lambda = 0.332$ $(\alpha = 3.35\%)$ used in this study. The domain confinement leads to the reduction of the fluid flow strength for all the fluid systems but it does not affect the deformation uniformly. These observations can be justified by considering the creeping flow solution. Briefly, the domain confinement affects the electric field and the flow field, and its influence on the deformation and maximum velocity can be formulated as $\mathcal{D} = C^e C_1^h \mathcal{D}_\infty$ and $U_{\max} = C^e C_2^h U_{\max_\infty}$. Here, $C^e = f(\widetilde{\sigma}, \lambda)$, $C_1^h = f_1(\widetilde{\mu}, \lambda)$, and $C_2^h = f_2(\widetilde{\mu}, \lambda)$, are coefficients that reflect on the modification of the electric and hydrodynamic forces by domain confinement, respectively. It is to be noted that these coefficients can be easily identified from the solution of Ref. [34]. For fluid systems $A - C$, the confinement effect reduces the hydrodynamic forces. Thus, C_1^h and C_2^h are lower than their corresponding values in an unbounded domain. However, the confinement effect increases the electric forces for fluid systems A and C, while it does the opposite for fluid system B. Accordingly, the net effect of the confinement is determined by the coefficients $C^e C_1^h$ and $C^e C_2^h$, compared to the corresponding ones for an unbounded domain. Here, $C^e C_2^h$ is less than that for an unbounded domain for fluid systems A–C. As such, $U_{\max} < U_{\max_\infty}$ uniformly. However, for fluid systems A and C, $C^e C_1^h$ is larger than that for an unbounded domain, while the opposite is true for fluid system B. Accordingly, $\mathcal{D} > \mathcal{D}_\infty$ for fluid systems B and C, while $|\mathcal{D}| < |\mathcal{D}_\infty|$ for fluid system A.

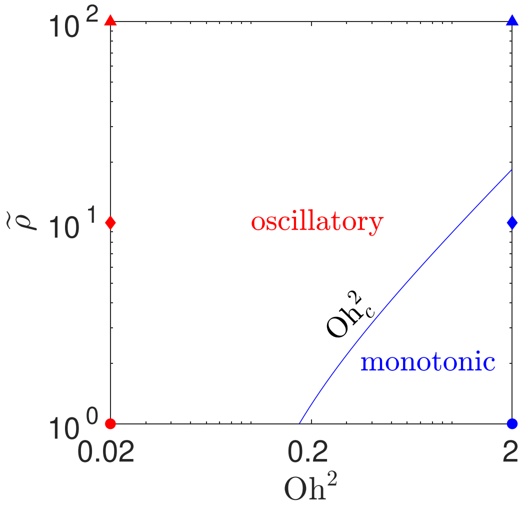

FIG. 16. A phase diagram depicting the regions of the monotonic and oscillatory responses in the physical space. The characteristic Ohnesorge number squared (Oh_c^2) is found from Eq. (16). The symbols represent the placement on the map of the high- and low-Oh^2 number simulations. Here the circle, diamond, and triangle represent the results of Figs. 13 and 14, respectively.

The confinement effect was explored by performing two extra simulations in cubic boxes of 1.5 and 2 a side, for each simulation that was presented so far. This led to volume fraction (confinement ratio) of $\alpha = 0.9929\%$ $(\lambda = 0.2149)$ and 0.4189% (0.1612), respectively. Recall that for the original simulations $\alpha = 3.35\%$ and $\lambda = 0.3224$, corresponding to a unit cubic box. Here, a highlight of these study is provided in Fig. 17, which shows the confinement effect for fluid system A and $\mathrm{Oh}^2 = 2$. For the top row, $\widetilde{\rho} = 1$, and for the bottom row, $\widetilde{\rho} = 100$. The deformation (in an absolute sense) increases with an increase in the domain size and the difference is more pronounced at steady state compared to the transient. However, the kinetic energy decreases with an increase in the domain size. Furthermore, the confinement effect on the kinetic energy is more pronounced than that on the deformation. The deformation for the intermediate domain is nearly the

TABLE VIII. Estimation of confinement effect for the three fluid systems used in this study, using creeping flow solution of Ref. [34]. The numbers in the parentheses show the percentage of the relative decrease or increase in $\mathcal{D}$ and $U_{\max}$ compared with the corresponding values in an unbounded domain.

Fluid System	$U_{\max}/U_{\max_\infty}$ (percent)	$\mathcal{D}/\mathcal{D}_\infty$ (percent)
A	0.963 (−3.7)	0.955 (−4.5)
B	0.9187 (−8.13)	1.001 (+0.1)
C	0.993 (−0.7)	1.03 (+0.7)

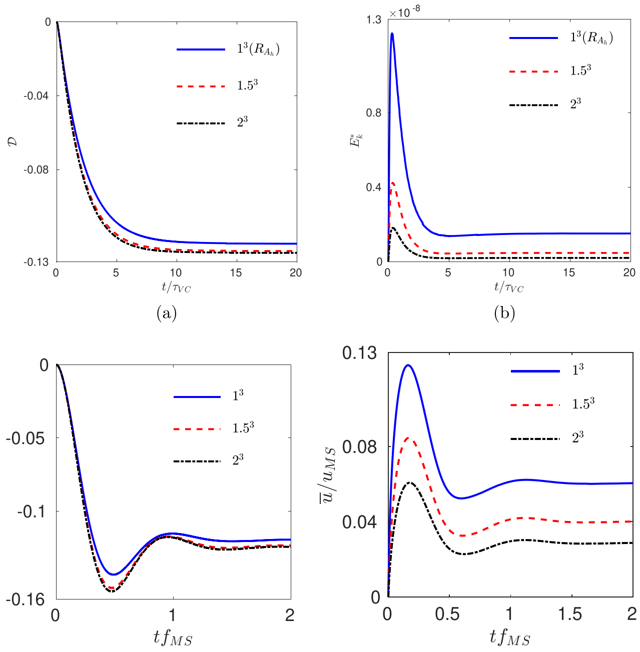

(a) (b)

(c) (d)

FIG. 17. Effect of confinement on the deformation and kinetic energy. The computational domains are cubes of sizes 1, 1.5, and 2, the fluid system is A, and $\text{Oh}^2 = 2$. For panels (a) and (b), $\widetilde{\rho} = 1$, and for panels (c) and (d), $\widetilde{\rho} = 100$. For panel (b), E_k is nondimensionalized by $\rho_o u_s^2 \Omega$, where $u_s \equiv u_{\text{EHD}} = \epsilon_o E_0^2 a/\mu_o$ and Ω is the box volume. $f_{\text{MS}} = \omega_{\text{MS}}/2\pi$ and the velocity scale is $u_{\text{MS}} = a f_{\text{MS}}$, where ω_{MS} is given in Eq. (B2b).

same as that for the large one, reflecting the fact that a cubic box of 1.5 a side can be considered essentially an unbounded domain for evaluating the deformation. The $\mathcal{D}$-λ correlation is in line with that for the creeping flows (Table VIII), while E_k-λ correlation is the opposite. The discrepancy between the numerical results and the creeping flow predictions concerning the kinetic energy is due to the convective effects, which are present in the numerical simulations but are absent in the creeping flow solution. This argument is backed by the fact that the effect of the domain confinement on the kinetic energy increases with an increase in the convective effects, as is evident by comparison of panels (b) and (d). For both panels, the convective term in the ambient is scaled by $\text{Re}_f = 0.1$. However, the convective term in the drop is scaled differently; it is $\widetilde{\rho}\text{Re}_f = 0.1$ and 10 for panels (b) and (d), respectively. The results for fluid systems B and C are not presented as they were similar to that for fluid system A.

F. Position of the maximum velocity

In the course of investigations of the fluid flow structure (Sec. V A 1), an interesting observation was made regarding the location of the steady-state maximum velocity for fluid system B [Fig. 5(f)]. Whereas Taylor's solution [1] predicts the location of the maximum velocity $U_{\max}$ [Eq. (A7)] to be at the drop surface and at polar angles $\theta = 45°$ and 135°, there, the maximum velocity occurred inside the drop somewhere along the poles. It is conjectured that this discrepancy is due to the consideration of the creeping flow solution beyond its range of applicability. Briefly, Taylor's solution for the velocity field is a zeroth order solution in a regular series solution in which the capillary number Ca is the perturbation parameter, $\mathbf{u} = \mathbf{u}_0 + \text{Ca}\mathbf{u}_1 + O(\text{Ca}^2)$. In this solution, the nondimensional velocity field $\mathbf{u}_0/U_{\max}$ inside and outside of the drop is only function of the nondimensional radial distance r/a and the polar angle θ. Accordingly, the location of the maximum velocity remains intact, regardless of the input parameters of the problem. The solution also predicts a smaller peak ($\approx 0.77 U_{\max}$) inside the drop along the poles at $r/a \approx 0.577$. However, examination of the Ajayi's solution [35], which is a first order solution to the problem, shows that the location and the magnitude of the maximum velocity are modified by the first order velocity $\mathbf{u}_1$. Since $\mathbf{u}_1$ is a function of the property ratios ($\widetilde{\sigma}$, $\widetilde{\epsilon}$, $\widetilde{\mu}$), capillary number Ca, and the degree of the drop deformation $\mathcal{D}$, all these parameters can affect the position of the maximum velocity in a real setting. In particular, they can reduce the surface velocity and increase the velocity along the poles, leading to the switch over of the position of the maximum velocity. As such, the observation made in Fig. 5(f), is not specific to region **II**. Detailed examination of this matter warrants a study of its own.

VI. CONCLUSIONS

Direct numerical simulations were performed to study some of the less explored aspects of the transient electrohydrodynamics of a liquid drop in DC electric fields I. The governing equations of the problem were solved using a parallelized front tracking/finite difference scheme in the framework of Taylor-Melcher's leaky dielectric theory. To account for the effects of the dielectric properties on the questions of interest, three representative fluid systems (Table II), corresponding to regions **I–III** of the deformation-circulation map were considered (Fig. 2). The drop deformed to an oblate in region **I** and a prolate in regions **II** and **III**. For density- and viscosity-matched reference simulations at high and low Oh^2 number, the deformation parameter and the flow field settled to a steady state. The steady-state flow field consisted of two toroidal vortices inside the drop (in the northern and southern hemispheres) that were matched with the corresponding vortices in the ambient fluid. The external flow ran from the poles toward the equator in regions **I** and **II**, while it ran in the opposite direction in region **III**.

It was shown that the instantaneous flow pattern was the result of the superposition of the deformation- and hydrodynamic shear-driven flow patterns, where the former was behind the generation of vortices that crossed into and out of the drop surface (the so-called open vortices in an unbounded domain), while the latter led to recirculating vortices that remained confined in each fluid. For high-Oh^2 reference simulations in which the drop deformed monotonically, the evolution of the flow field consisted of two stages, the acceleration stage and the deceleration stage. In the acceleration stage, the deformation rate was increasing with time ($\partial^2\mathcal{D}/\partial t^2 > 0$), and thus, the flow pattern was mainly shaped by the deformation-driven vortices. These vortices gradually penetrated into the drop for all the fluid systems. In the deceleration stage, the deformation rate was decreasing with time ($\partial^2\mathcal{D}/\partial t^2 < 0$), and thus, the shear-driven vortices gradually became dominant. In this stage, the deformation-driven vortices gradually retreated to the ambient fluid for fluid systems A and C, while they continued to move into the drop for fluid system B. For all the fluid systems, the evolution of the vortices continued until the flow field settled to its steady state. The underlying reason for the difference in the paths was attributed to the difference in senses of the deformation- and shear-driven vortices for fluid systems A and C compared to those for fluid system B.

The evolutions of the deformation parameter $\mathcal{D}$, the kinetic energy E_k, and the deformation rate $\partial\mathcal{D}/\partial t$ with time for the high- and low-Oh^2 reference simulations led to a number of observations. For both cases, the deformation rate controlled the kinetic energy, while the kinetic energy controlled the deformation. Because of the close association of the deformation rate with the instantaneous deformation, this hinted a two-way coupling between the deformation rate and the kinetic energy. For the high-Oh^2 reference simulations, the deformation increased (in an absolute sense) monotonically until it settled to a steady state. However, the kinetic energy had an overshoot early on and then gradually settled to a steady state. Here, the dynamic response resembled that of an overdamped mechanical system. For the low-Oh^2 reference simulations, the evolutions of both the deformation and the kinetic energy were oscillatory. Here, the dynamic response resembled that of an underdamped mechanical system. Furthermore, the oscillation frequency of the deformation was close to that predicted by Miller-Scriven ($f_{\rm MS} = \omega_{\rm MS}/2\pi$).

The effect of the density ratio on the dynamic response and the fluid flow strength was studied for both the high and the low Oh^2 reference simulations. For the former, no tangible changes in the dynamic response and the average velocity were observed when the density ratio was increased from 1 to 10. However, when the density ratio was increased from 10 to 100, both parameters transitioned from a monotonic response to an oscillatory one. For all the cases, the steady-state deformation and the average velocity remained intact. For the latter, the dynamic response was oscillatory at all the density ratios. The oscillation frequency, nondimensionalized by the Miller-Scriven frequency, was essentially the same for all the density ratios, reflecting the fact that the Miller-Scriven frequency was the intrinsic frequency. The oscillation amplitude increased with an increase in the density ratio. The fluid flow strength, represented by the average velocity (15) was oscillatory and correlated positively with the density ratio $\widetilde{\rho}$.

The confinement effect on the deformation and the kinetic energy was explored by performing two simulations in cubic boxes of sizes 1.5 and 2, for every original simulation (which was done in a unit box). Examination of the selected results for fluid system A showed that the deformation (in an absolute sense) correlated positively with confinement while the kinetic energy did the opposite. These observations were attributed to the modification of the electric and hydrodynamic forces by the confinement and their interplay in setting the drop deformation and the fluid flow generation. The confinement effect was more pronounced on the kinetic energy, compared to the deformation; whereas the deformation remained essentially the same when the domain size was increased from 1.5 to 2, the kinetic energy for the two systems had noticeable differences.

APPENDIX A: HYDRODYNAMIC SHEAR- AND DEFORMATION-DRIVEN COMPONENTS OF THE CREEPING FLOW SOLUTION

In what follows the result of recasting the solution of Ref. [5] in a new form is reported. This is done to highlight the role of the deformation rate on the evolution of the flow field. Briefly, for quasi steady-state creeping flows, the equation of motion is $-\boldsymbol{\nabla} p + \mu\nabla^2\mathbf{u} = \mathbf{0}$, which has the following solution in terms of stream function:

$$\psi_i = (A_i r^3 + B_i r^5)\sin^2\theta\cos\theta, \tag{A1a}$$

$$\psi_o = (A_o r^{-2} + B_o)\sin^2\theta\cos\theta. \tag{A1b}$$

Here, the unknown coefficients are time-dependent and determined from the interfacial jump conditions. Application of the jump conditions results in

$$A_i = \underbrace{\frac{16\widetilde{\mu}+19}{15(\widetilde{\mu}+1)}\frac{\partial\mathcal{D}}{\partial t}}_{\text{deformation-driven}} + \underbrace{\frac{1}{5(\widetilde{\mu}+1)}\frac{\widetilde{[\![\tau^e_{r\theta}]\!]}}{\mu_o}}_{\text{shear-driven}}, \tag{A2a}$$

$$B_i = -\underbrace{\frac{2\widetilde{\mu}+3}{5(\widetilde{\mu}+1)a^2}\frac{\partial\mathcal{D}}{\partial t}}_{\text{deformation-driven}} - \underbrace{\frac{1}{5(\widetilde{\mu}+1)a^2}\frac{\widetilde{[\![\tau^e_{r\theta}]\!]}}{\mu_o}}_{\text{shear-driven}}, \tag{A2b}$$

$$A_o = -\underbrace{\frac{(3\widetilde{\mu}+2)a^5}{5(\widetilde{\mu}+1)}\frac{\partial\mathcal{D}}{\partial t}}_{\text{deformation-driven}} + \underbrace{\frac{a^5}{5(\widetilde{\mu}+1)}\frac{\widetilde{[\![\tau^e_{r\theta}]\!]}}{\mu_o}}_{\text{shear-driven}}, \tag{A2c}$$

and

$$B_o = \underbrace{\frac{(19\widetilde{\mu}+16)a^3}{15(\widetilde{\mu}+1)}\frac{\partial\mathcal{D}}{\partial t}}_{\text{deformation-driven}} - \underbrace{\frac{a^3}{5(\widetilde{\mu}+1)}\frac{\widetilde{[\![\tau^e_{r\theta}]\!]}}{\mu_o}}_{\text{shear-driven}}, \tag{A2d}$$

where the deformation rate $\partial\mathcal{D}/\partial t$ needs to be determined. In Eq. (A2), $\widetilde{[\![\tau^e_{r\theta}]\!]}$ is the coefficient of $\sin 2\theta$ in the electric shear stress

$$[\![\tau^e_{r\theta}]\!] = \frac{9\epsilon_o E_\infty^2}{2(\widetilde{\sigma}+2)^2}(\widetilde{\epsilon}-\widetilde{\sigma})\sin 2\theta. \tag{A3}$$

The deformation $\mathcal{D}$ is found from the solution of the normal stress balance equation

$$\tau\frac{\partial\mathcal{D}}{\partial t} + \mathcal{D} = \underbrace{\frac{a}{8\gamma}\left(\widetilde{[\![\tau^e_{rr}]\!]} - \frac{3}{5}\frac{3\widetilde{\mu}+2}{\widetilde{\mu}+1}\widetilde{[\![\tau^e_{r\theta}]\!]}\right)}_{\mathcal{D}_{\rm ss}}, \tag{A4}$$

where $\widetilde{[\![\tau^e_{rr}]\!]}$ is the coefficient of $\cos^2\theta$ in the electric pressure

$$[\![\tau^e_{rr}]\!] = \frac{9\epsilon_o E_\infty^2}{2(\widetilde{\sigma}+2)^2}[\widetilde{\epsilon} - 1 + (\widetilde{\sigma}^2 + 1 - 2\widetilde{\epsilon})\cos^2\theta]. \tag{A5}$$

In Eq. (A4), τ is the characteristic timescale that governs the dynamics, and $\mathcal{D}_{\rm ss}$ is the steady-state deformation. Solution of

Eq. (A4) leads to

$$\mathcal{D} = \mathcal{D}_{\mathrm{ss}}[1 - \exp(-t/\tau)], \tag{A6a}$$

$$\tau = \frac{\mu_o a}{\gamma} \frac{(19\widetilde{\mu} + 16)(2\widetilde{\mu} + 3)}{40(\widetilde{\mu} + 1)}, \tag{A6b}$$

which suggests that the drop deformation settles monotonically to its steady-state value.

Inspection of the radial and tangential velocity components shows that during the transient, the maximum fluid velocity occurs at the poles (where the radial velocity u_r is maximum) or at the surface at $\theta = \pi/4$ and $3\pi/4$ (where the tangential u_θ velocity is maximum). The radial velocity u_r is driven solely by $\partial\mathcal{D}/\partial t$. As such, it will cease to exist at steady state. The tangential velocity is due to both $\partial\mathcal{D}/\partial t$ and $[\![\tau^e_{r\theta}]\!]$ during the transient, but it will be driven solely by $\tau^h_{r\theta}$ at steady state. The tangential surface velocity at steady state is $u_\theta = U_{\max} \sin 2\theta$, where

$$U_{\max} = \frac{9}{10} \frac{u_s}{1 + \widetilde{\mu}} \frac{\widetilde{\sigma} - \widetilde{\epsilon}}{(\widetilde{\sigma} + 2)^2}, \tag{A7}$$

is the maximum velocity in the flow field.

APPENDIX B: CHARACTERIZING THE OSCILLATORY DYNAMIC RESPONSE

Reference [12] developed an equation for the deformation of a liquid drop in DC electrics field using the solution of Ref. [32] for small-amplitude free oscillation of a liquid drop

$$\mathcal{D} = \mathcal{D}_\infty \left[1 - \exp(-\zeta t) \left(\cos \omega_{\mathrm{MS}} t + \left(\frac{\zeta}{\omega_{\mathrm{MS}}} \right) \sin \omega_{\mathrm{MS}} t \right) \right], \tag{B1}$$

where

$$\omega_{\mathrm{MS}} = \omega_{\mathrm{L}} - \frac{25(\omega_{\mathrm{L}} \mu_i \mu_o \rho_i \rho_o)^{1/2}}{2^{1/2} \Lambda}, \tag{B2a}$$

$$\zeta = \frac{25(\omega_{\mathrm{L}} \mu_i \mu_o \rho_i \rho_o)^{1/2}}{(2^{1/2})\Lambda} - \frac{625 \mu_i \mu_o \rho_i \rho_o}{\Lambda^2} + \frac{5[6\mu_i^2 \rho_i + 16\mu_o^2 \rho_o + \mu_i \mu_o (4\rho_i - \rho_o)]}{2a^2 \Gamma[(\mu_i \rho_i)^{1/2} + (\mu_o \rho_o)^{1/2}]^2}, \tag{B2b}$$

$$\omega_{\mathrm{L}} = \sqrt{\frac{24}{3\widetilde{\rho} + 2} \left(\frac{\gamma}{\rho_o a^3} \right)}, \tag{B2c}$$

$$\Lambda = 2a\Gamma[(\mu_i \rho_i)^{1/2} + (\mu_o \rho_o)^{1/2}], \tag{B2d}$$

$$\Gamma = 2\rho_o + 3\rho_i. \tag{B2e}$$

In Eq. (B2), ω_{L} is the natural frequency of oscillation at the inviscid limit [31], and ζ is the damping factor. This equation is valid for $\mathrm{Oh}_i^2,\ \mathrm{Oh}_o^2 \ll 1$, $\mu_i,\ \mu_o \ll 1$, and $O(\mu_i) = O(\mu_o)$.

---

[1] G. Taylor, Proc. R. Soc. London A **291**, 159 (1966).
[2] J. R. Melcher and G. I. Taylor, Annu. Rev. Fluid Mech. **1**, 111 (1969).
[3] E. Lac and G. Homsy, J. Fluid Mech. **590**, 239 (2007).
[4] C. Sozou, Proc. R. Soc. London A **334**, 343 (1973).
[5] A. Esmaeeli and P. Sharifi, Phys. Rev. E **84**, 036308 (2011).
[6] J. A. Lanauze, L. M. Walker, and A. S. Khair, Phys. Fluids **25**, 112101 (2013).
[7] J. Zhang, J. D. Zahn, and H. Lin, Phys. Rev. E **87**, 043008 (2013).
[8] D. Das and D. Saintillan, J. Fluid Mech. **810**, 225 (2017).
[9] P. M. Vlahovska, Annu. Rev. Fluid Mech. **51**, 305 (2019).
[10] J. Q. Feng and T. C. Scott, J. Fluid Mech. **311**, 289 (1996).
[11] H. Nganguia, Y.-N. Young, A. T. Layton, M.-C. Lai, and W.-F. Hu, Phys. Rev. E **93**, 053114 (2016).
[12] A. Esmaeeli and A. Behjatian, J. Fluid Mech. **893**, A26 (2020).
[13] R. J. Haywood, M. Renksizbulut, and G. D. Raithby, AIChE J. **37**, 1305 (1991).
[14] G. Supeene, C. R. Koch, and S. Bhattacharjee, J. Comput. Theor. Nanosci. **1**, 429 (2004).
[15] G. Supeene, C. R. Koch, and S. Bhattacharjee, J. Colloid Interface Sci. **318**, 463 (2008).
[16] T. Ward and G. Homsy, Phys. Fluids **13**, 3521 (2001).
[17] S. Lee, D. Im, and I. Kang, Phys. Fluids **12**, 1899 (2000).
[18] T. Ward and G. Homsy, J. Fluid Mech. **547**, 215 (2006).
[19] C. Christov and G. Homsy, Phys. Fluids **21**, 083102 (2009).
[20] N. Kaji, Y. Mori, and Y. Tochitani, J. Heat Transfer **107**, 788 (1985).
[21] P. K. Notz and O. A. Basaran, J. Colloid Interface Sci. **213**, 218 (1999).
[22] R. T. Collins, K. Sambath, M. T. Harris, and O. A. Basaran, Proc. Natl. Acad. Sci. **110**, 4905 (2013).
[23] A. Fernandez, G. Tryggvason, J. Che, and S. L. Ceccio, Phys. Fluids **17**, 093302 (2005).
[24] G. Tryggvason, B. Bunner, A. Esmaeeli, D. Juric, N. Al-Rawahi, W. Tauber, J. Han, S. Nas, and Y.-J. Jan, J. Comput. Phys. **169**, 708 (2001).
[25] M. A. Halim and A. Esmaeeli, FDMP: Fluid Dyn. Mater. Process. **9**, 435 (2013).
[26] A. Esmaeeli, Phys. Fluids **28**, 073306 (2016).
[27] A. Esmaeeli and G. Tryggvason, Phys. Fluids **17**, 093303 (2005).
[28] G. I. Taylor, Proc. R. Soc. London A **146**, 501 (1934).
[29] O. Vizika and D. Saville, J. Fluid Mech. **239**, 1 (1992).
[30] M. N. Reddy and A. Esmaeeli, Int. J. Multiphase Flow **35**, 1051 (2009).
[31] H. Lamb, *Hydrodynamics* (Cambridge University Press, Cambridge, 1932).
[32] C. Miller and L. Scriven, J. Fluid Mech. **32**, 417 (1968).
[33] J. Sherwood, J. Fluid Mech. **188**, 133 (1988).
[34] A. Esmaeeli and A. Behjatian, Phys. Rev. E **86**, 036310 (2012).
[35] O. O. Ajayi, Proc. R. Soc. London A **364**, 499 (1978).